# POLITECNICO DI TORINO

## Laser Powder Bed Fusion of AISI 316L–BN Metal Matrix Composites: Processability and Microstructural Analysis


**Department of Applied Science and Technology**

**Master of degree program in**
**Materials Engineering for Industry 4.0**

**Supervisor:**

Prof. Abdollah Saboori

**candidate:**

Zeinab Jafari


**A.Y. 2024/2025**

## Acknowledgements

I would like to sincerely express my deepest gratitude to my esteemed supervisor, Dr. Sabouri. Throughout this journey, his patience, guidance, and generous sharing of invaluable experience have played a fundamental role in shaping and completing this work. Without his constant presence and unwavering support, reaching this point would not have been possible. Working with him has been an unforgettable experience and one of the most rewarding aspects of my academic life an experience that will always remain in my memory and in my heart. For all of this, I am profoundly grateful.

I am also deeply thankful to my beloved husband, who has stood by my side through every step of this journey. Whenever challenges discouraged me, his calming presence and encouraging words gave me strength and rekindled my motivation to continue. His endless patience and understanding throughout this project have been an invaluable blessing, making this difficult path smoother and more bearable. His presence in my life is truly priceless, and I am proud and grateful to have him by my side.

I am sincerely grateful to my family, who, through their selflessness, have always been the wings that lifted me and the foundation upon which I could pursue my goals. Their constant prayers and unwavering support have been an inexhaustible source of hope and motivation. They have taught me to always strive and never leave any task unfinished. Without a doubt, their presence has made my life more meaningful, beautiful, and fulfilling.

I would also like to thank my colleagues and friends, whose support, encouragement, and thoughtful conversations not only enriched my research but also made the entire experience far more enjoyable. Finally, I am deeply grateful to the faculty and staff of the Integrated Additive Manufacturing Laboratory at Politecnico di Torino. The resources, facilities, and welcoming environment you provided were essential in carrying out this research, and your support played a key role in making this work possible

## Abstract

Laser Powder Bed Fusion (L-PBF) is an advanced additive manufacturing (AM) technique that allows the production of complex metal parts with high precision and design freedom. Beyond shaping complex geometries, it also opens the door to developing new alloys and reinforced composites. AISI 316L stainless steel is one of the most widely used materials in L-PBF because of its excellent corrosion resistance, toughness, and ductility. AISI 316L stainless steel is widely adopted in Laser Powder Bed Fusion (L-PBF) due to its corrosion resistance, strength, and ductility, its relatively low hardness and limited wear resistance remain critical drawbacks in demanding applications. In this study, we investigate the use of hexagonal boron nitride (h-BN) as a reinforcing phase to overcome these limitations in L-PBF processed 316L. Microstructural characterization using optical microscopy (OM) revealed significant variations in porosity, while scanning electron microscopy (SEM) highlighted modifications in grain morphology and the occurrence of solidification cracks that often formed along grain boundaries due to the rapid cooling characteristic of L-PBF. X-ray diffraction (XRD) confirmed the formation of secondary phases linked to BN addition, and X-ray computed tomography (XCT) provided a detailed view of internal porosity, showing a clear increase as BN content rose. In this study, we examined the use of hexagonal boron nitride (h-BN) as a reinforcing phase to overcome these limitations in L-PBF processed 316L. Microstructural analysis using optical microscopy (OM) highlighted variations in porosity, while scanning electron microscopy (SEM) revealed changes in grain morphology, along with solidification cracks that often formed along grain boundaries due to the rapid cooling characteristic of L-PBF. X-ray diffraction (XRD) confirmed the formation of secondary phases linked to BN addition, and X-ray computed tomography (XCT) provided a detailed view of internal porosity, showing a clear increase as BN content rose. Mechanical testing confirmed that h-BN incorporation significantly improved performance. Both nanoindentation and wear tests showed notable gains in hardness and wear resistance, demonstrating the reinforcing effect of BN. These findings suggest that h-BN is an effective additive for enhancing the strength and durability of L-PBF AISI 316L stainless steel, broadening its potential for use in more demanding engineering applications.

Key words: Additive manufacturing, Powder bed fusion, Stainless steel, Microstructure, Mechanical Property, Boron nitride.

# Table of Contents

## Table of Abbreviations

| Abbreviation | Definition |
|---|---|
| 3D | Three-Dimensional |
| AM | Additive Manufacturing |
| BJ | Binder Jetting |
| BN | Boron Nitride |
| BSE | While The Backscattered Electron |
| CAD | Computer-Aided Design |
| CJP | Color Jet Printing |
| CNT | Carbon Nanotube |
| CT | X-Ray Computed Tomography |
| DED | Only The Direct Energy Deposition |
| DLP | Digital Light Projection |
| DMD | Direct Metal Deposition |
| DOD | Drop On Demand |
| EB-PBF | While Electron Beam PBF |
| EBM | Electron Beam Melting |
| EDX | Energy Dispersive X-Ray Spectroscopy |
| FCC | Face-Centered Cubic |
| FDM | Fused Deposition Modeling |
| FFF | Fused Filament Fabrication |
| HAZ | Heat-Affected Zone |
| HIP | Hot Isostatic Pressing |
| L-PBF | Laser Powder Bed Fusion |
| LMD | Laser Metal Deposition |
| LOM | Laminated Object Manufacturing |
| LPBF | Laser Powder Bed Fusion |
| MEX | Material Extrusion |
| MJ | In Material Jetting |
| NDT | Non-Destructive Testing |
| NH3 | Ammonia |
| OM | Optical Microscopy |
| PBF | Powder Bed Fusion |

| | |
|---|---|
| PSD | Particle Size Distribution |
| RTP80-TL90 | Profilometer |
| SE | Secondary Electron |
| SEM | Scanning Electron Microscopy |
| SL | Sheet Lamination |
| SLA | Stereolithography |
| SLM | Selective Laser Melting |
| SLS | Selective Laser Sintering |
| STL | Standard Tessellation Language |
| UAM | Ultra Sonic Additive Manufacturing |
| VP | Vat Photo-Polymerization |
| W-EDM | Wire Electrical Discharge Machining |
| WEDM | Wire Electrical Discharge Machining |
| XCT | X-Ray Computed Tomography |
| XRD | X-Ray Diffraction |
| h-BN | Hexagonal Boron Nitride |

# Tables

# Figures

# 1. Introduction

Additive manufacturing (AM), particularly laser-based additive manufacturing (LAM), represents a modern production approach in which components are built layer by layer directly from a CAD model. Over the past decade, this technology has attracted considerable industrial interest as a distinctive alternative to traditional manufacturing routes. Its strengths lie in enabling rapid prototyping and product customization, ensuring efficient use of raw materials, and allowing the fabrication of highly complex structures that would otherwise be challenging to achieve using conventional methods. [1], [2]

Powder Bed Fusion (PBF) has emerged as one of the most AM technologies, based on a high-energy laser to selectively fuse thin layers of powder spread across a substrate. This technique enables the production of both metallic and non-metallic components with significant precision, extending its relevance well beyond conventional manufacturing applications and it is used in aerospace and automotive, energy sectors and prototyping design. Importantly, PBF also provides a platform for developing novel material systems tailored to specific performance requirements. Among its key advantages is the ability to fabricate homogeneous alloy parts with enhanced mechanical properties, while at the same time supporting freedom in design through the creation of complex geometries and near-net-shape components and minimizing the material utilization. This not only reduces or even eliminates the need for extensive post-machining but also shortens the overall production chain.[3], [4], [5]

However, several challenges remain. Technology is constrained by limited build volumes, the high cost of equipment and powders, and the high thermal gradients generated during processing. These gradients often lead to rise in residual stress, which can promote crack formation and compromise the integrity of the final component.[6]

The quality and reliability of parts produced by Laser Powder Bed Fusion (L-PBF) strongly depend on the careful selection and control of process parameters. [7] Key factors such as laser power, scan speed, hatch spacing, and their combined effect often expressed as volumetric energy density (VED) directly influence the melting behavior, microstructure, and final properties of the material. In addition, the scanning strategy plays a critical role in distributing heat uniformly, thereby reducing residual stress and minimizing the risk of defects such as porosity or cracking. Also important is the characterization of the feedstock powder, like particle size distribution, shape, and flowability have a significant effects layer deposition and consolidation. To maintain stability of process and prevent oxidation, the operation is typically carried out under an inert gas atmosphere, most commonly Argon. With the optimized balance of these parameters and conditions, it becomes possible to overcome the inherent challenges of the technique and achieve dense, high-quality components with desirable mechanical performance.[8], [9], [10], [11]

Stainless steel 316 is among the most widely utilized materials in Laser Powder Bed Fusion (L-PBF) owing to its excellent corrosion resistance, high strength, ductility, and toughness, which make it suitable for demanding structural and functional applications. However, stainless steel 316L can

exhibit relatively low strength under specific conditions, along with limited wear resistance, which narrows its suitability for more demanding engineering applications.[12] To overcome these limitation, researchers have previously reinforced stainless steel 316L with particles such as silicon carbide (SiC), graphene, and titanium nitride (TiN), all of which have shown improvements in mechanical properties and microstructural refinement. Building on this foundation, the present study introduces hexagonal boron nitride (h-BN) as a novel reinforcement. h-BN possesses unique physicochemical characteristics that can enhance the microstructure, improve load-bearing capability, and improve the mechanical performance, offering a promising pathway to overcome the intrinsic limitations of 316 stainless steel in additive manufacturing. [3], [13], [14], [15]

# 2. State of the art

## 2.1. Additive Manufacturing

Additive manufacturing (AM) refers to a manufacturing approach in which materials are built up layer by layer to create objects from three-dimensional (3D) model data, in contrast to traditional subtractive methods that remove material to form the final shape[16].

In AM, the production process usually follows a clear sequence of steps. It starts with designing the part in 3D using Computer-Aided Design (CAD) software, which includes all essential details such as geometry, internal structures, and supports, which are carefully defined to ensure accuracy and functionality. The design is then converted into a standard tessellation language (STL) file, a format widely used to make it compatible with printing systems. This file is uploaded to the machine or slicing software, which breaks the 3D model into thin 2D layers and generates the tool path or G-Code that will guide the printer. Before the building begins, key parameters like part orientation, layer thickness, and any additional features are set. Once printing starts, the machine takes over, with duration depending on the size and complexity of the part. Human involvement during this phase is minimal, limited mostly to monitoring the process to ensure everything runs smoothly.[17], [18], [19]

Once the printing process is completed, the manufactured parts are carefully removed from the building chamber. Depending on the additive manufacturing technique, additional steps such as debinding or sintering may be required to achieve full material densification. To further enhance the quality and performance of the components, various post-processing operations may be applied.[20] Machining is often applied to improve dimensional accuracy and surface finish, while heat treatment serves to relieve residual stress and optimize mechanical properties. Finally, non-destructive testing methods are employed to verify structural integrity without compromising the part itself. Together, these stages ensure that the final components not only meet design specifications but also demonstrate the reliability and performance needed for their intended applications.[21], [22]

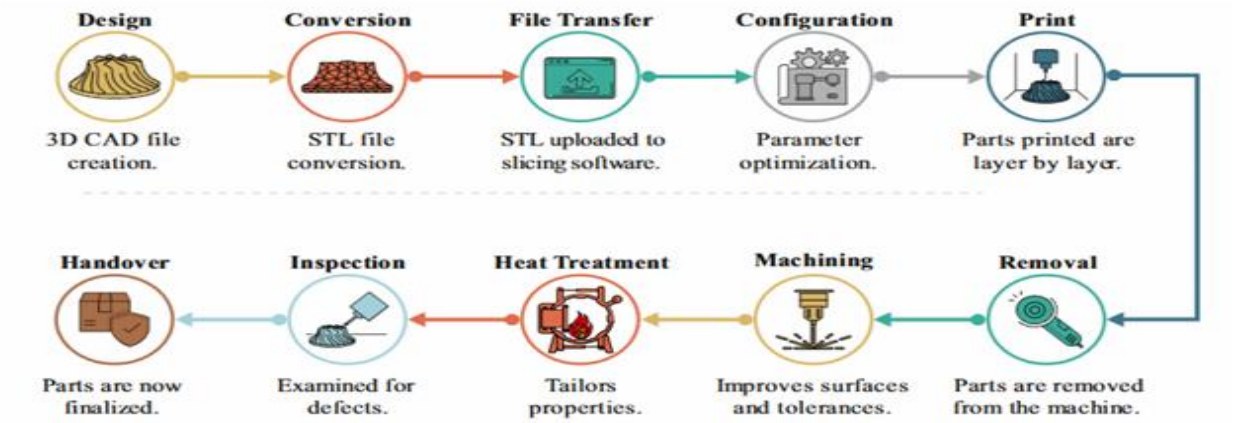


*Figure 1: Schematic general workflow of additive manufacturing methods[23]*

A wide range of materials can be used in additive manufacturing, each chosen to suit a specific application. These Commonly used material classes include polymers, metals, ceramics, composites, and even bio-based substances [24], [25]. Depending on the specific additive manufacturing technology, the raw material may be provided in the form of powders, liquid resins, or solid filaments [26]. This adaptability has supported the growing use of AM across a wide range of industries, most notably in aerospace, automotive, biomedical, energy and advanced manufacturing, where tailored material selection is crucial to achieving high-performance components [27],[28], [29], [30]

Additive manufacturing provides several advantages over conventional production methods, it enables high material efficiency by reducing waste, shortens lead times, and contributes to more resilient supply chains by minimizing the reliance on extensive tooling or machining. The technology is well suited for producing novel, high-performance prototypes, repairing traditionally manufactured components, and facilitating reverse engineering. Its capacity to create intricate geometries in a single build process encourages design innovation, while its flexibility makes it both cost-effective for small batch runs and ideal for fabricating customized parts tailored to specific applications [31], [32], [33]. However, limitations include machine build size, increased specific energy consumption, higher raw material cost, and initial capital investment, often produces rough surface finishes requiring post-processing.[33], [34]

### 2.1.1. Classification of Additive Manufacturing

According to the ASTM classification, additive manufacturing (AM) technologies are divided into seven distinct categories, as shown in Table 1.[35]

Sheet Lamination (SL) involves bonding thin sheets of material, often metals, typically through welding. This method offers relatively low cost and good surface quality compared to other additive manufacturing techniques. Vat Photopolymerization (VP) employs a liquid photopolymer that is selectively cured layer by layer using a UV light source. It provides high build speed and excellent surface resolution, though it is associated with very high costs. Material Jetting (MJ) works by depositing droplets of polymers or waxes that are subsequently cured with UV light, resulting in components with smooth surfaces but generally low mechanical strength.[36] Binder Jetting (BJ) relies on spreading a thin layer of powder, onto which a print head selectively applies a binding agent. While it works with many different materials, the parts it produces often contain relatively high porosity. Directed Energy Deposition (DED) feeds powder or wire through a nozzle, where it is melted by a focused energy source during deposition. This method is particularly useful for repairing damaged parts, though it often requires additional post-processing. Material Extrusion (MEX), widely recognized through its application in fused filament fabrication (FFF), involves extruding thermoplastic material through a heated nozzle and depositing it layer by layer to build the part. It allows for multi-material printing but generally produces parts with poor surface finish. Finally, Powder Bed Fusion (PBF) spreads a layer of powder across a build platform, selectively melting or sintering areas with a concentrated energy source. Collectively, these seven methods

represent the core additive manufacturing techniques for producing components [37], [38],[38] [39], [40]

*Table 1: Classification of Additive Manufacturing according to ISO/ASTM*

| AM Process | Short Description | Material | Form | Techniques | REF |
|---|---|---|---|---|---|
| **Powder bed fusion (PBF)** | Thermal energy fuses Regions of a powder bed | Metals Polymers ceramic | Powder | Selective laser sintering (SLS) Electron Beam Melting (EBM) Selective laser Melting (SLM) | [41] |
| **Material extrusion (MEX)** | Material dispensed through a nozzle | Polymers ceramic | Filament Pellets Paste | Fused deposition modeling (FDM) Fused filament Fabrication (FFF) | [42], [43] |
| **Vat Photo-Polymerization (VP)** | Liquid photo polymer in a Vat is cured by light | Photopolymers | Liquid | Stereolithography (SLA) Digital light projection (DLP) | [44] |
| **Material jetting (MJ)** | Droplets of material are Selectively deposited | Polymers waxes | Liquid | Drop on Demand (DOD) Poly jet Nano particle Jetting (NPJ) | [36], [45] |
| **Binder jetting (BJ)** | A liquid bonding agent is Selectively deposited | Metal | Powder | 3D printing(3DP) Color Jet Printing (CJP) | [46], [47] |
| **Sheet lamination (SL)** | Sheets of material are Bonded | Metals polymers | Sheet | Laminated object Manufacturing (LOM) Ultra Sonic Additive Manufacturing (UAM) | [48], [49] |
| **Directed energy Deposition (DED)** | Focused thermal energy Used to fuse materials by Melting when depositing | Metals polymers ceramic | Powder Wire | Laser Metal Deposition (LMD) Direct Metal Deposition (DMD) | [38], [50], [51] |

Laser-based additive manufacturing is a process in which a laser is used as the energy source to selectively fuse materials by melting or sintering them, this can be achieved from a powder bed or through direct material deposition. [52]. Out of these 7 classes of techniques, only the direct energy deposition (DED) and powder bed fusion (PBF) categories make use of laser energy source for fusion of the material, that are being widely developed for fabricating complex shapes of metals and alloys[35].

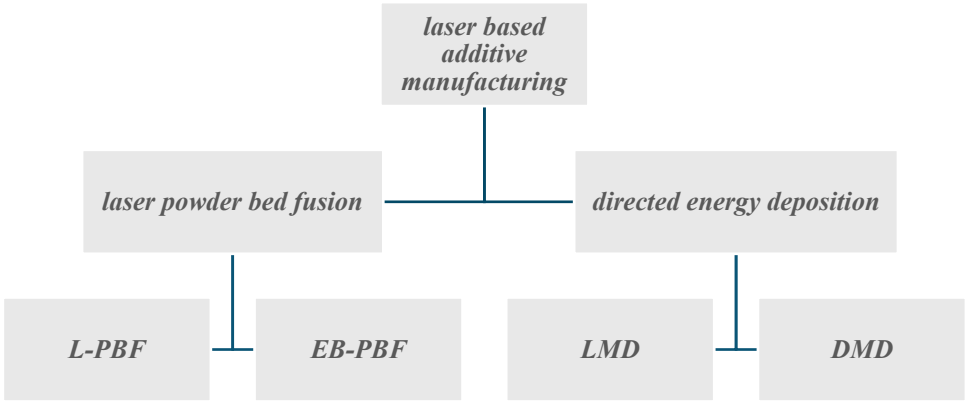


Figure 2: laser based Additive Manufacturing categories.

#### 2.1.1.1. Directed Energy Deposition

Directed Energy Deposition (DED) process is an Additive Manufacturing (AM) process, in which a focused thermal energy is used to fuse materials by melting as they are being deposited, by melting them during layer-by-layer deposition.[53] in this method, the material is melted using a concentrated heat source, which may be provided by a laser, an electron beam, or a plasma/electric arc. The energy source is focused on a specific location, enabling the feedstock to be deposited directly onto the substrate (for the initial layer) or onto the previously built layer. This localized energy input generates a melt pool by fusing both the incoming material and the underlying layer, with solidification upon cooling forming the deposition bead.[54]

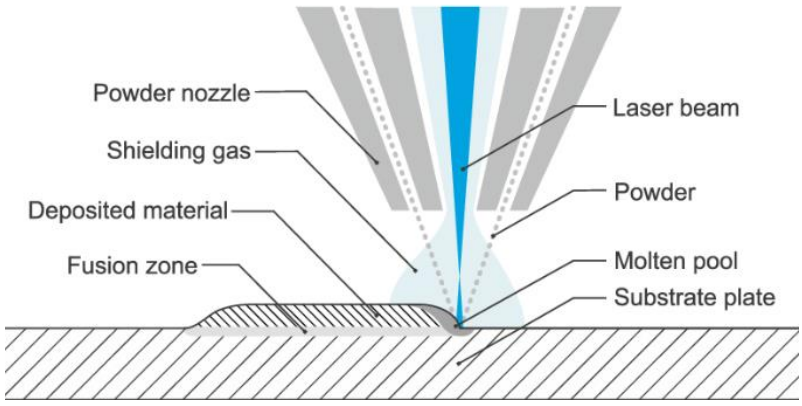


*Table 2: schematic of the DED technique.*

The feedstock material can be fed in the form of powder or filament that is shown in Figure 3. When interaction with the energy source, the material melts almost instantly, creating a melt pool that then

solidifies rapidly once the energy input moves away. To transition from a single-point deposition to a continuous additive process, a steady supply of material is required.[55]

In DED, the building chamber is not restricted, since the material is delivered directly to the deposition. This design provides greater versatility compared to chamber-limited processes, and an inert gas shield can be applied during printing to minimize oxidation of the material.[56]

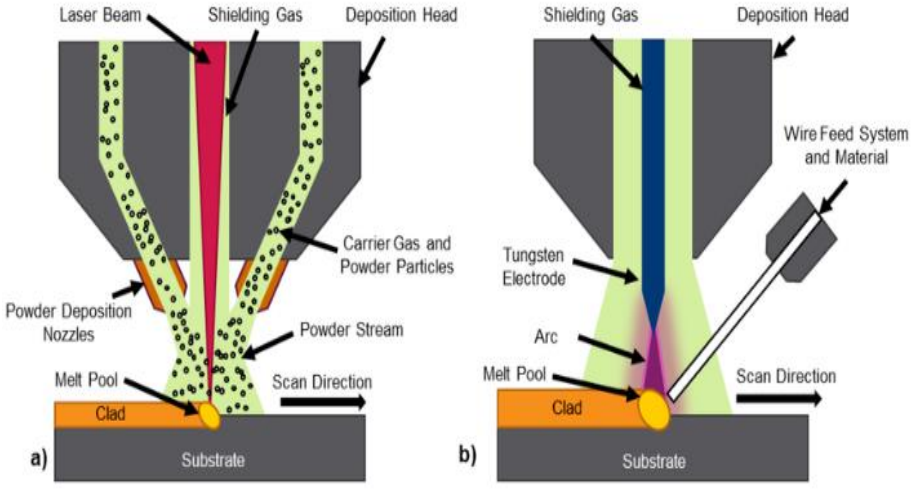


*Figure 3: Schematic illustration feed stock of DED system. (a) Powder feed; (b) Wire feed[57]*

Directed Energy Deposition (DED) provides several benefits to be one of the most versatile of the existing AM process. This process can handle a variety of materials including titanium, nickel, iron alloys, and stainless steel, achieving higher deposition rates than most other AM methods. In addition, it generally results in a comparatively smaller heat-affected zone (HAZ) than conventional welding-based repair approaches[58] With its relatively high deposition rate and freedom from small chamber constraints, DED is best applicable for automotive and aerospace component repair and remanufacturing, as it enables the restoration of damaged and broken parts by depositing lost material and reshaping them to their initial geometry. [59] In addition to this, the process allows for the fabrication of functionally graded materials, enabling the combination of different alloys in a single build, and supports material efficiency by generating less waste than conventional subtractive manufacturing. [54]

While DED offers notable advantages, it also has certain limitations that limit its broader application. The process generally produces components with a lower dimensional accuracy and relatively rough surface finish compared to L-PBF, making post-processing steps like machining or polishing necessary. The high thermal gradients inherent to DED can lead to residual stresses, microstructural inhomogeneities, and, if not well controlled, defects such as porosity or cracking. [60]Moreover, the complexity of synchronizing the energy source, material feed, and shielding gas increases equipment

and process demands. Finally, DED is less suited for fabricating intricate geometries or fine structural details, which limits its applicability in domains where high precision and complex small-scale features.[61], [62]

### 2.1.1.2. Powder Bed Fusion

Laser Powder Bed Fusion (L-PBF), also known as Selective Laser Melting (SLM), is an additive manufacturing process in which a high energy laser selectively fuses metal powder particles in a layer-by-layer manner to form fully dense solid parts. Technology belongs to the broader family of AM techniques and can be employed for the fabrication of both metallic and ceramic parts[63]. Figure 4 shows the working principle of a PBF machine.

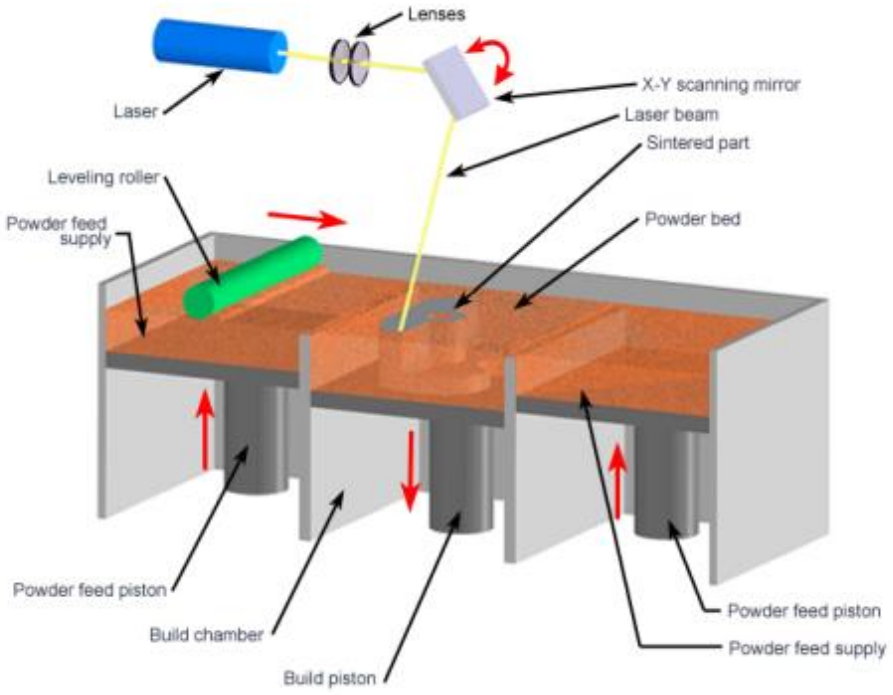


*Figure 4: Schematic illustration describing the operating principle of the SLM [64]*

protected by the flow of inert gas, commonly argon or nitrogen to minimize oxidation during processing. Beyond preventing oxidation, the gas stream also helps to remove the condensate that is produced by melting the powder, homogeneous gas flow across the build area plays an important role in the quality and properties of SLM-processed parts. Before the laser exposure, the powder bed is preheated to a material specific temperature to reduce thermal gradients and improve process

stability. When preheated, a thin and uniform powder layer is spread over the platform using a recoater blade or roller, preparing the surface for the subsequent melting step.[65], [66]

In the subsequent stage, the energy source that is commonly a high-power laser or, in some cases, an electron beam selectively scans the powder bed, melting and consolidating the material according to the geometry defined by the digital CAD model. This controlled melting ensures that the newly fused material bonds with the previously built layer form a metallurgical bond and part of the three-dimensional structure. After each scan, the build platform is lowered by a predefined layer thickness, and a fresh layer of powder is uniformly spread across the surface through the recoating mechanism. This sequence of powder deposition, selective melting, and solidification is repeated iteratively until the entire component is fabricated layer by layer.[67]

When the building is completed, the chamber is allowed to cool, after which the unfused powder is carefully removed during the depowdering phase. The excess material is collected, sieved when necessary, and returned to the storage system for reuse in future builds. Once the part is fabricated, it is typically subjected to post-processing treatments to enhance both its mechanical properties and surface quality. These treatments may involve stress-relief heat treatment, removal of support structures, machining, surface finishing, or advanced densification techniques such as hot isostatic pressing (HIP). Together, these steps ensure that the final component achieves the desired performance standards. Selective Laser Melting (SLM) offers numerous advantages that make it a highly attractive option for advanced manufacturing applications. One of its key strengths is the exceptional design freedom it provides, enabling the fabrication of intricate geometries, lattice structures, and lightweight components that would be extremely difficult or prohibitively expensive to achieve using conventional methods. As a near-net-shape process, SLM also ensures high material efficiency by minimizing waste and allowing unused powder to be recycled for future builds.[68]

In terms of performance, SLM can produce parts with densities often exceeding 99.5%, while the rapid solidification inherent to the process refines the microstructure, thereby enhancing hardness and strength. This reliability makes SLM particularly suitable for critical applications. Technology also supports a high level of customization, making it ideal for small-batch or specialized production; for instance, patient-specific medical implants or lightweight aerospace components. Moreover, complex assemblies can be consolidated into a single build, reducing the need for welding or mechanical joining and thereby improving structural integrity. [71] [69], [70]

Finally, SLM is compatible with a broad range of materials, including stainless steels, aluminum alloys, titanium, and nickel-based superalloys, further expanding its applicability across industries where precision, performance, and innovation are essential. [72].[73]

At the same time, SLM is not without its challenges. Technology requires expensive equipment, high-quality powders, and strict safety measures for handling fine metallic particles, all of which raise production costs. Build sizes are limited by the machine chamber, and the process is relatively slow compared to conventional mass-production methods. Moreover, the rapid heating and cooling cycles generate strong thermal gradients that can cause residual stress, warping, or cracking,

especially in alloys with poor weldability. As-built parts also tend to have rough surfaces and often need additional machining or polishing. For these reasons, SLM is best applied where its unique capabilities such as design freedom, high performance, and customization, justify the extra cost and processing effort.[69], [70]

### 2.1.1.3. Process Parameters

In Laser Powder Bed Fusion (L-PBF), the quality of the manufactured part is strongly influenced by the laser parameters, as they directly determine the amount and distribution of energy delivered to the powder bed. Parameters such as laser power, beam diameter, scan pattern, and hatch spacing play a critical role in shaping the scanning behavior and controlling the stability of the melt pool. Since L-PBF is fundamentally a thermal process, its performance and outcomes are largely dictated by a set of critical processing parameters, including:[74]

Parameters such as laser power, spot size, and hatch spacing strongly influence the effective scanning speed and, consequently, the stability of the melt pool. For instance, higher power or a smaller beam diameter can generate deeper and more stable melt pools, but if combined with low scanning speeds, they may cause overheating, balling, or keyhole porosity. On the other hand, insufficient energy input due to low power or excessive scanning speed often results in lack of fusion and high porosity, compromising the mechanical integrity of the part.[75], [76], [77]

Because SLM is essentially a thermal process, the balance among processing parameters is crucial. The laser beam power (W), scanning speed (mm/s), hatch spacing (mm), powder layer thickness (mm), and spot size (mm) collectively define the volumetric energy density supplied to the material. This energy density dictates whether the powder fully melts and consolidates or remains partially bonded. Too high of an energy density leads to defects such as evaporation and distortion, whereas too low of an energy density causes incomplete melting and poor interlayer bonding. Thus, Careful optimization of these parameters is therefore essential to ensure proper fusion, achieve high density, and produce components with smooth surfaces while minimizing process instabilities.[78], [79], [80]

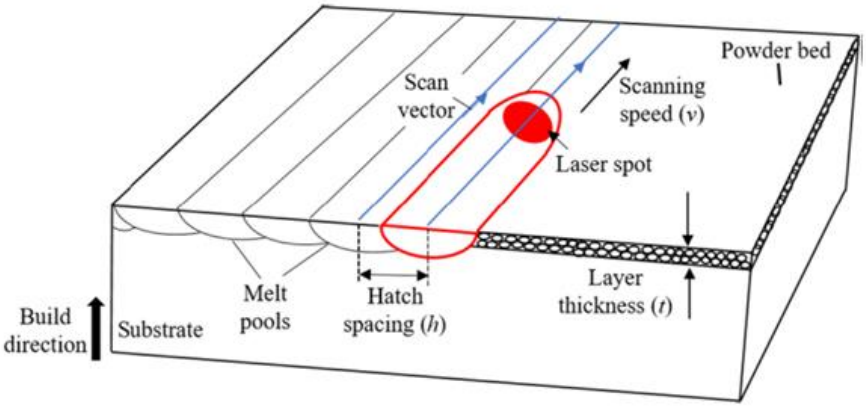

*Figure 5: laser-related process parameters in L-PBF process*

A keyway to describe this balance is through the concept of volumetric energy density, which combines laser power, scan speed, hatch spacing, and layer thickness into one parameter that expresses the energy supplied per unit volume of material. Achieving the right energy density is essential to ensure proper fusion between particles and layers, as well as to control the microstructure and surface finish of the final part. It combines the main process parameters into a single expression:[81] [82]

$$\text{VED} = \frac{\text{P}}{\text{v.h.l}}$$

Where:

VED= Volumetric energy density $[\frac{J}{mm^3}]$

P = Laser power $[W]$

v =Scanning speed $[\frac{mm}{s}]$

h = Hatching distance [mm]

l = Layer thickness [mm]

Additionally, scanning strategies such as stripes, chessboard, or rotational patterns play an important role in distributing heat and residual stress across the build. Optimized scanning strategies prevent excessive heat accumulation in localized regions, reducing the risk of warping or cracking, especially in alloys sensitive to thermal gradients. By alternating the scanning direction between layers or subdividing the exposure area, residual stress buildup can be mitigated, leading to improved dimensional accuracy and uniform microstructure. In summary, achieving high-quality SLM parts requires not only selecting appropriate values for individual parameters but also coordinating them in a holistic manner to balance energy input, thermal gradients, and stress distribution[83][84]

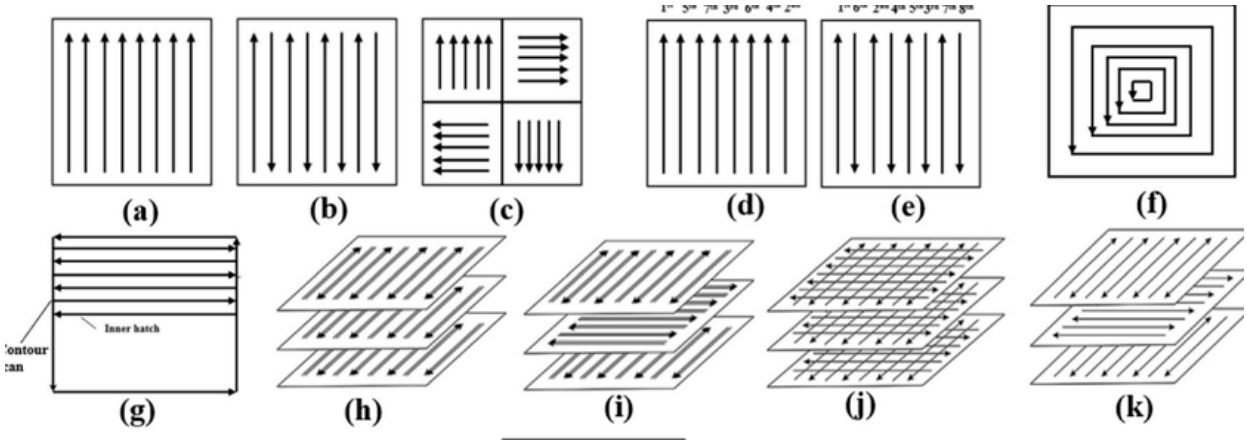


*Figure 6: Schematic of different types of scanning strategies[85]*

Overall, producing high-quality SLM parts requires not only the careful selection of individual parameter values but also their coordinated adjustment in a holistic way, ensuring a balance between energy input, thermal gradients, and stress distribution. Well-designed scanning strategies further contribute by promoting uniform heat distribution, which reduces residual stress and helps to minimize warping or cracking.[86]

Alongside the laser-related parameters, other factors such as powder layer quality, build plate temperature, and protective gas environment also strongly affect the process. Smooth, evenly spread powder layers improve density and surface finish, while preheating the build plate can reduce thermal stress. An inert gas atmosphere, typically argon or nitrogen, prevents oxidation and helps remove spatter generated during melting. Together, these process parameters form a delicate balance: fine-tuning them allows manufacturers to achieve high-density, reliable parts with tailored microstructures, while poor control can lead to defects, poor mechanical properties, and build failures.[87]

## 2.2. Stainless Steel and Composition

Stainless steel 316L is an austenitic chromium–nickel–molybdenum alloy with low carbon content. Its typical chemical composition is shown on the table. The presence of molybdenum enhances corrosion resistance, particularly against chlorides and reducing acids, while the low carbon concentration minimizes the risk of carbide precipitation during welding, improving resistance to intergranular corrosion. This careful balance of alloying elements gives 316L its excellent durability, making it one of the most versatile and reliable stainless steels for demanding applications.

*Table 3: Chemical composition of 316L austenitic stainless steel powder (wt.%).[88]*

| Element | Fe | Cr | Ni | Mo | Mn | Si | C |
|---|---|---|---|---|---|---|---|
| **% wt** | Bal. | 16.0-18.0 | 10.0 -14.0 | 2.0-3.0 | 2.00 | < 1.00 | < 0.03 |

stainless steel 316L exhibits a stable austenitic microstructure with face-centered cubic (FCC) crystals, which contributes to its excellent toughness, ductility, and non-magnetic behavior in the annealed state. When processed by conventional methods or advanced manufacturing routes such as Laser Powder Bed Fusion (LPBF), it typically shows fine grains with uniform distribution of alloying elements. This fine microstructure improves both strength and corrosion resistance. The alloy is known for its high corrosion resistance in marine and chemical environments, good mechanical strength (yield strength around 170–310 MPa in annealed condition), and excellent ductility and toughness even at cryogenic temperatures. It also maintains good weldability and formability, making it suitable for both traditional and additive manufacturing processes.

*Table 4: data sheet [89], [90], [91]*

| Physical properties | metric | comment |
|---|---|---|
| Density | 7.98 g/cm³ | |
| Hardness (HB) | 215 | |
| Tensile Strength, Ultimate | 515 MPa | |
| Tensile Strength, Yield | 205 MPa | |
| Hardness, Brinell | 149 | Estimated from Rockwell C |
| Hardness, Rockwell B | 80 | Estimated from Rockwell C |
| Hardness, Vickers | 155 | Estimated from Rockwell C |
| Tensile strength | 500-700 N/mm² | |
| Modulus of elasticity | 165- 200kN/mm2 | 20-500 |
| Thermal conductivity | | |
| Coefficient of linear thermal expansion | 16.0-18.0 $10^{-6}$ $K^{-1}$ | at 100-500 C |
| Specific Thermal Capacity | 500 J/kg K | at 20°C |
| Modulus of Elasticity | 165-200 kN/mm2 | at 20-500 C |
| Thermal Conductivity | 15 W/m K | At 20 C |
| Yield strength | 200 N/mm² | |
| Electrical Resistivity | 0.75 Ω mm²/m | |
| Melting Point | 1375-1400 | |

Because of this combination of properties, stainless steel 316L is widely used across industries where both durability and corrosion resistance are essential. In the medical sector, it is used for surgical implants, orthopedic devices, and dental instruments due to its biocompatibility. In the chemical and petrochemical industries, it serves in equipment exposed to harsh environments, such as heat exchangers, pressure vessels, and piping systems. In the marine sector, it is applied to pumps, valves, and components exposed to seawater. Additionally, it finds use in aerospace, food processing, and energy industries, as well as in advanced fields like additive manufacturing, where it is one of the most common powders employed in SLM/LPBF due to its processability, mechanical reliability, and corrosion resistance.

### 2.2.1. Limitations of 316L and Improvement Methods

Although stainless steel 316L is well regarded for its excellent corrosion resistance, good ductility, and reliable mechanical performance, it still presents limitations that restrict its application in highly demanding environments. Its relatively low hardness and limited wear resistance reduces its suitability for components exposed to severe abrasion. Similarly, while its strength is proper for many environments, it does not reach the high strength-to-weight ratios required in advanced aerospace or energy systems. In additive manufacturing, 316L typically solidifies into a fine yet conventional austenitic microstructure, which, despite its stability, does not inherently provide the enhanced functionality or tailored properties needed for next-generation, high-performance components.[92]

One approach to overcome these limitations is through in-situ alloying during the Laser Powder Bed Fusion (LPBF) process. Instead of relying solely on pre-alloyed powders, additional elements can be blended directly into the powder bed or feedstock, allowing new compositions to form during laser melting. This approach allows for the adjustment of mechanical strength, hardness, and corrosion behavior by influencing the solidification pathway and resulting microstructure. [93] The addition of copper into AISI 316L stainless steel through in-situ alloying during L-PBF has been reported to refine the microstructure and improve mechanical performance. The Cu atoms dissolve into the Fe matrix, forming a stable austenitic structure. Compared with conventional 316L, the modified alloy exhibits columnar grains with finer cellular structures. Mechanical testing revealed enhanced strength, with an ultimate tensile strength of 558 MPa, yield strength of 510 MPa, and elongation of 30.4%. These improvements are attributed to solid solution strengthening and cellular refinement.[94]. Another study has shown that the incorporation of Al (below 1.8 wt%) into austenitic stainless steel enables the formation of versatile microstructures with exceptional mechanical properties. The Al-modified alloy exhibits yield strengths up to 1338 MPa (approximately 1.7 times higher than conventional austenitic stainless steels) due to B2 precipitation within metastable δ-ferrite grains. Retaining partial austenite maintains ductility, while localized precipitation strengthening during LPBF allows for tailored mechanical performance.[95]

Another promising strategy is the fabrication of metal matrix composites (MMCs) in situ during the printing process. By addition of ceramic reinforcements such as SiC, TiC, $Al_2O_3$, or graphene into the stainless steel matrix, it is possible to combine the toughness and ductility of 316L with the hardness and wear resistance of ceramics. The laser not only melts the base alloy but also promotes reactions at the metal–ceramic interface, leading to the formation of well-bonded composites. This strategy has the potential to markedly improve the performance of 316L, enabling its use in applications that demand higher wear resistance, customized mechanical properties, or even multifunctional behavior.

### 2.2.2. Metal Matrix Composites Based on Stainless Steel 316L

MMC is an advanced material formed by combining a metal or alloy as the matrix with a reinforcing phase, typically ceramics such as carbides, oxides, or nitrides, but also in the form of particles, fibers, or whiskers. The concept is to leverage the ductility, toughness, and electrical/thermal conductivity of metals, while introducing the strength, hardness, stiffness, and wear resistance provided by reinforcements. [96]This synergy results in materials with superior mechanical and functional properties compared to conventional alloys, making MMCs highly attractive for demanding applications. Metal matrix composites (MMCs), whether used as coatings or in bulk, are drawing growing interest because they can significantly enhance the performance of metals.[97] [98], [99]

But in the Laser Powder Bed Fusion (LPBF) method, powders should be gas-atomized to ensure high purity, controlled size distribution, and good flowability. In this process, the shape of the reinforcement particles is critical: preferably spherical, as spherical particles spread more uniformly during recoating, flow more easily, and help reduce porosity in the final part. In contrast, irregular or sharp-edged powders tend to flow poorly and can cause non-uniform reinforcement distribution. The size of the reinforcement should typically be between the 10–50 μm range, comparable to the 316L stainless steel matrix powder. Oversized particles may not melt properly, leading to weak bonding, while excessively fine powders can agglomerate and oxidize easily. Another key factor is compatibility with SLM, since the reinforcement must withstand the intense localized laser energy without decomposing or in some cases, be able to react in a controlled way to form in-situ reinforcements like TiC or $TiB_2$. Finally, the distribution of reinforcement within the steel matrix must be homogeneous, which requires careful powder preparation. Common approaches include ball milling, mechanical alloying, or wet mixing, all of which are used to ensure uniform dispersion of the ceramic or carbon-based phases before the LPBF process[92].[100]

#### 2.2.3. Challenges and Solutions for Processing SS316L-Based Metal Matrix Composites

When using SS316L as the metal matrix in powder bed fusion (PBF) to produce metal matrix composites (MMCs), several key challenges must be addressed. One of the most significant issues

is the poor wettability between SS316L and typical ceramic reinforcements, such as SiC or $Al_2O_3$, which can lead to weak interfacial bonding and compromised mechanical performance. Additionally, the large difference in thermal expansion coefficients between SS316L and ceramic reinforcements often results in residual stresses and microcracks during cooling. Porosity and incomplete fusion are also common concerns in the additive manufacturing of SS316L-based MMCs, especially when reinforcements disrupt the melt pool dynamics. Powder segregation poses another major challenge, as SS316L is much denser than most reinforcement particles, making it difficult to achieve uniform distribution during powder preparation. Moreover, even when the powders are well mixed, reinforcement particles can migrate during laser scanning due to melt pool turbulence, leading to non-uniform reinforcement dispersion in the final part. Overcoming these challenges requires a combination of approaches, such as coating reinforcement particles to improve wettability, optimizing laser parameters to ensure full densification, employing advanced mixing techniques to prevent segregation, and considering post-processing treatments to relieve residual stresses. [101]

*Table 5: Challenges and Solutions for SS316L-Based MMCs via SLM*

| Challenge | Potential Solutions |
|---|---|
| **Poor wettability** | - Surface coating of reinforcement particles (Ni, Ti)<br>Alloying SS316L to improve wetting<br>- In-situ reinforcement formation |
| **Thermal mismatch** | - Careful selection of reinforcement material<br>- Post-processing heat treatment- Use of functionally graded materials |
| **Porosity and lack of fusion** | - Optimization of SLM parameters (laser power, scan speed)<br>- Use of pre-alloyed or homogenized powders<br>- Hot isostatic pressing (HIP) |
| **Powder segregation** | - Mechanical alloying or ball milling<br>- Binder-assisted mixing<br>- Matching particle size distributions |
| **Reinforcement distribution control** | - Use of finer reinforcement particles<br>- Optimized scan strategies<br>- Process monitoring & melt pool control |

### 2.2.4. process optimization

Although L-PBF provides great design freedom, it is a highly complex process due to Multiphysics interactions in the powder bed and melt pool. Producing high-quality parts depends on carefully optimizing parameters such as laser power, scan speed, hatch spacing, layer thickness, scanning strategy, atmosphere, and powder bed temperature. Since testing all combinations is impractical, ranking these parameters by importance helps streamline design of experiments and improve material properties like density. [102]

The quality of parts produced by PBF strongly depends on the proper selection of process parameters. An unsuitable combination of laser power and scanning speed may cause defects such as lack-of-fusion porosity, keyhole formation, or the balling effect. When the scanning speed is too high relative to the applied laser power, the energy input becomes insufficient to fully melt the powder, leading to incomplete fusion and weak bonding between successive layers. Conversely, excessive laser power at a given scanning speed can cause overheating and excessive penetration into the powder bed, which may trap shielding gas and generate keyhole porosity. Such conditions can also remelt or disturb previously solidified regions, resulting in undesirable microstructural alterations. Increasing both power and speed within the safe processing window helps to reduce these defects. However, increasing the power and speed beyond this range will also lead to an unstable melt pool behavior and formation of small spherical balls known as balling phenomenon which leads to discontinuous melt tracks.[103], [104]

Optimization of selective laser melting (SLM) parameters has been extensively studied for 316L stainless steel due to their strong influence on microstructure and mechanical properties. Using the Taguchi method, the influence of key process parameters, including laser power, scan speed, layer thickness, and hatch spacing was systematically evaluated with respect to relative density, tensile strength, and elongation. The analysis revealed that scan speed exerted the greatest influence on relative density (42.38%), whereas laser power was the most significant factor governing tensile strength (31.17%) and elongation (45.67%). Regression modeling further validated these findings, demonstrating strong predictive capability with coefficients of determination exceeding 80% for all responses. [105]Another study on SLM of 316L stainless steel reinforced with 5 vol.% $CeO_2$ demonstrated that optimizing the laser scanning speed, while keeping other parameters constant. can produce highly dense composites. Although the $CeO_2$ addition did not change the phase formation, it significantly refined the microstructure, leading to enhanced strength without compromising ductility. These results highlight the importance of scanning speed in optimizing composite properties and suggest potential for high-temperature applications.[106]

### 2.2.5. Reinforcement of Mechanical Properties

In recent work, carbon nanotube (CNT) reinforced 316L stainless steel composites have been produced by laser powder bed fusion (LPBF), with attention given to microstructure, hardness, and wear performance. The addition of 1 wt% CNT refined the microstructure, shifting the solidification mode from cellular/columnar to nanoscale dendritic growth. Although most CNTs were damaged during processing, carbon segregation along cellular and dendritic boundaries enhanced boundary strengthening. This led to improved hardness and a significant reduction in wear rate, with the wear mechanism changing from adhesive/abrasive in pure AM 316L to adhesion and oxidative wear in CNT/316L composites.[107]

In another study a dense and ultrafine-grained austenitic matrix reinforced with uniformly distributed nano-sized particulates was achieved by tailoring SLM parameters and adding 3 wt% submicron $V_8C_7$ ceramic particles into 316L powder via ball milling. Compared with SLM-printed 316L, the composites exhibited higher density, refined microstructure, and significantly improved tensile performance, with over 90% of grains smaller than 2 μm and an ultimate tensile strength above 1400 MPa, more than twice that of pure 316L. The strengthening was attributed to rapid nonequilibrium solidification during SLM, dispersion of carbide reinforcements, nanoscale nucleation effects of $V_8C_7$, and inhibition of austenite grain growth by particles at grain boundaries.[108]

*Table 6: Common reinforcement materials used in Stainless Steel 316L matrix composites, highlighting their families (carbides, nitrides, oxides, carbon-based, and borides) and the key improvements they provide.*

| | Reinforcement | Content | Objective |
|---|---|---|---|
| **Carbide** | TiC | 15 vol% | Micro Hardness<br>Microstructure |
| | V8C7 | 3wt% | Formation Mechanism<br>Strengthening |
| **Nitride** | TiN | 1,5,10 wt% | Mechanical Property |
| **Oxide** | Al2O3 | 1,2,3 wt% | Microstructure<br>Mechanical Properties |
| | CeO2 | 5% wt | Process Optimization,<br>Mechanical Properties |
| **Borides** | TiB2 | 0, 5, 10 %wt | Mechanical Properties,<br>Corrosion Resistance |
| **Carbon-Based** | graphene | 0.2 wt % | Mechanical Properties<br>Corrosion Resistance<br>Microstructure |
| | Carbon nanotube | 1 wt% | Microstructure<br>Wear Resistance |

Studies on graphene-reinforced stainless steel nanocomposites have shown that adding 0.2 wt% multilayer graphene nanosheets to 316L stainless steel significantly enhances densification and strength. At a volumetric energy density of 240 J/mm³, the material achieved 94.7% ± 0.5 relative density and ~1165 MPa tensile strength. Microscopic analyses attributed these improvements to graphene–steel interactions, in situ nano-inclusions, and dislocation pinning within cellular sub-grains. Energy density modulation was identified as a key factor in tailoring microstructure and texture for improved mechanical performance.[109]

## 2.3. Boron Nitride

Boron nitride (BN) is a chemical compound formed by the combination of boron and nitrogen.

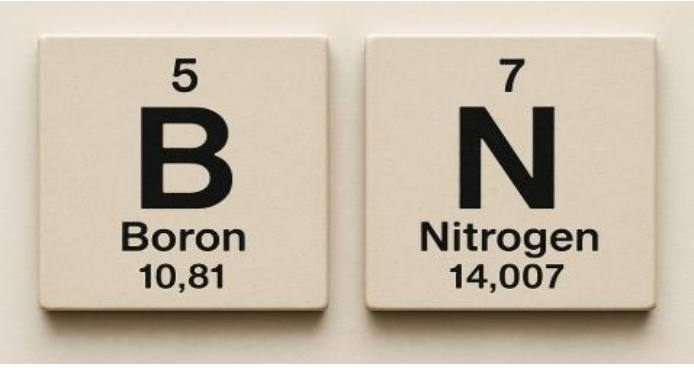


*Figure 7: Boron and Nitrogen elements*

BN is obtained by feeding $N_2$ gas in a vacuum chamber at high temperature. Boron is adjacent to carbon and nitrogen elements in the periodic table. These elements are known as the basic components for BN thin films. Reported that BN is produced by creating a reaction of boron trichloride (BCl3) and ammonia (NH3) [110] as described by the reaction equation below:

$$BCI3 + NH3 \rightarrow BN(s) + 3HCl$$

Boron Nitride has five allotropes in addition to these: turbotrain BN (t-BN), explosive BN (e-BN), rhombohedral BN (r-BN), amorphous BN (a-BN) and wurtzite BN (w-BN). Crystal structure of BN allotropes There are two main allotropes of boron nitride with outstanding properties, which are commonly known as hexagonal boron nitride (h-BN) and cubic boron nitride (c-BN).

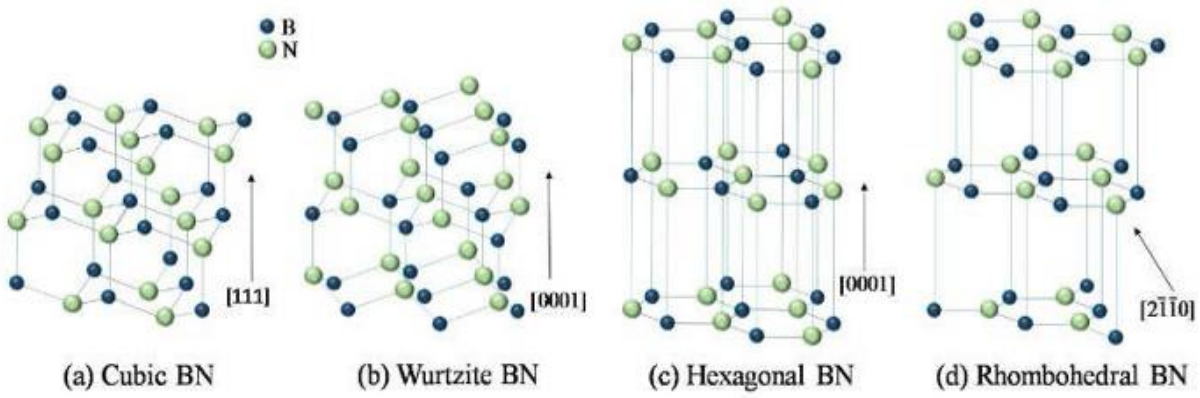


*Figure 8: Crystal structures of rhombohedral a) cubic boron nitride (c-BN), b) wurtzite BN (w-BN), c) hexagonal boron nitride (h-BN), d) rhombohedral BN (r-BN).[111]*

### 2.3.1. Properties

Hexagonal boron nitride (h-BN) has a graphite-like layered structure, where the sheets are bonded strongly within the plane but held together weakly between layers. This gives it excellent lubricating properties and makes it soft and easily machinable. h-BN has a white color and a good electrical insulator with 5.2 eV direct gap value, but a very good thermal conductor, stable up to high temperatures and resistant to oxidation up to about 1000 °C in air. Thanks to this unique combination of insulation, thermal stability, and mechanical strength, h-BN is widely used in lubricants, protective coatings, electrical insulators, composites, and as separators or additives in energy storage devices.[112], [113], [114]

Cubic boron nitride (c-BN), by contrast, has a diamond-like three-dimensional structure, which makes it the second hardest known material after diamond, it has 45-55GPa hardness, and its elastic modulus is also 850 GPa. It possesses high thermal conductivity; it has a wide band gap of Eg=6.4 eV. And has thermal stability up to about 1200 °C in air, and high melting temperature (2973°C). excellent chemical resistance, especially since it does not react with ferrous materials. Although electrically insulating, c-BN's extreme hardness and durability make it valuable in cutting and grinding tools, wear-resistant coatings, and high-power electronic applications. This combination of superior mechanical and thermal properties establishes c-BN as one of the most technologically important superhard materials.[115], [116], [117]

In the table are shown the physical properties of c-BN, h-BN:

*Table 7: properties of h-bn and cBN*

| Properties | h-BN | cBN | |
|---|---|---|---|
| Density | 2.1 | 3.45 | g/Cm3 |
| Bulk Modulus | 36.5 | 400 | GPa |
| Thermal Conductivity | 600 | 740 | w/M.K |
| Thermal Expansion | 2.7 $10^{-6}$c | 1.2 | $10^{-6}$ C |
| Melting Point | 2973 | 3246 C | C |
| Band Gap | 5.9- 6.4 | 10.1- 10.7 | (Ev) |

### 2.3.3. Applications

Hexagonal boron nitride (h-BN) is valued in a wide range of industries due to its unique combination of properties; it can resist very high temperatures, it is chemically inert, and it works as an excellent lubricant while still being electrically insulating. Energy Storage Applications: Hexagonal boron nitride (h-BN), an isoelectric analog of graphite, is limited to Li-ion battery anode due to its poor electrical conductivity, but its insulation nature and mechanical strength make it valuable as a separator component or electrode additive. Through functionalization, structural modification, and composite integration, h-BN has found applications in energy storage systems, including supercapacitors and rechargeable lithium batteries.[118], [119] Hexagonal boron nitride (h-BN) has attracted significant attention as a substrate and dielectric layer in nano-electronic devices due to its excellent electrical insulation, atomically smooth surface, and compatibility with two-dimensional materials. Beyond electronics, their high thermal conductivity makes it valuable in thermal applications, where it enhances heat dissipation and improves thermal management in advanced systems. h-BN also shows remarkable corrosion and chemical resistance, supporting its use in harsh environments and in high-temperature conditions. Commercially, h-BN has already been adopted in several industries, most notably as ceramic fillers to optimize the thermal conductivity of polymers, which are widely applied in electrical insulation for consumer electronics such as batteries and high-performance components. By blending with plastics, resins, and adhesives, h-BN helps improve both heat management and structural reliability. Furthermore, its stability at high temperatures, resistance to radiation, and chemical inertness make h-BN highly promising in nuclear engineering, where it is used to line reactor neutron shells and is considered for the first wall of thermonuclear reactors. Its proven role in aerospace, combined with ongoing research in emerging fields, highlights h-BN as both commercially viable and forward-looking material for critical technologies.[120], [121], [122], [123]

# 3. Materials and Methods

## 3.1. Materials

Gas-atomized AISI 316L stainless steel powder**,** composed of spherical particles with an average 10-63 μm served as the matrix material and the hexagonal boron nitride (h-BN) powder with particle size of < 1 μm . were used as the reinforcing phase at concentrations of 0.1 and 0.3 wt%. The stainless steel and h-BN powders were blended using a jar milling process without grinding media to avoid particle deformation. Mixing was performed under low-energy conditions for 12 hours to promote a homogeneous dispersion of the reinforcement within the 316L matrix.

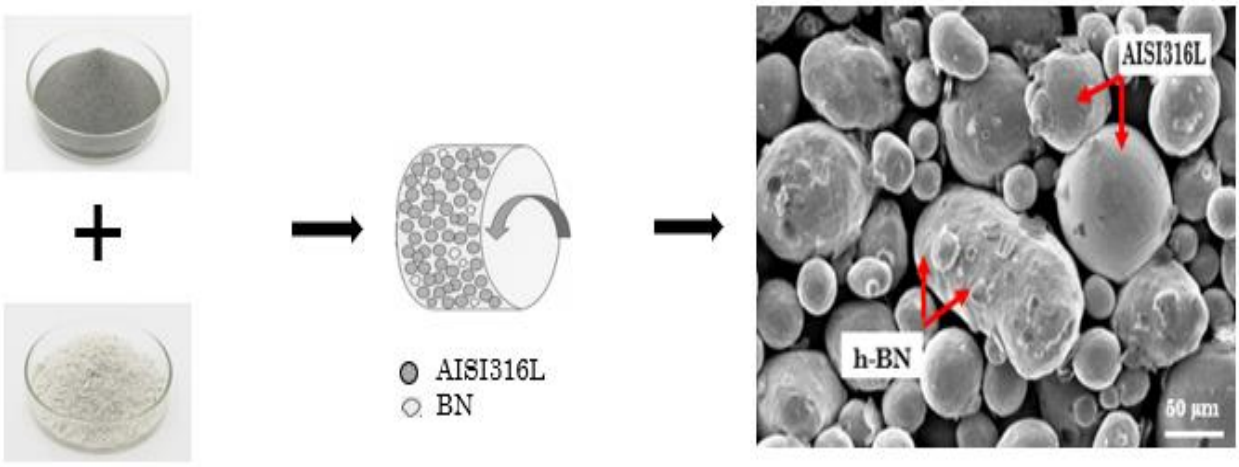


*Figure 9: Schematic illustration of jar milling used to mix BN and SS316L powders without milling balls. The jar rotation enables homogeneous blending of the powders*

## 3.2. Sample Modeling

in additive manufacturing, the part is initially created in computer-aided design (CAD) software, where its geometry and dimensions are specified. Then digital model is transformed into a standard tessellation language (STL) file, which represents the geometry through a triangular mesh and provides the required input for slicing and machine processing [124]

Sample modeling was performed using Materialize Magics software to generate the CAD files, while the fabrication was carried out in the Corso Terena Center of Politecnico di Torino. The process began with the design and preparation of the CAD models, which were used to produce six cubic specimens on each building platform. The precise dimensions of the fabricated samples are illustrated in Fig 10.

.

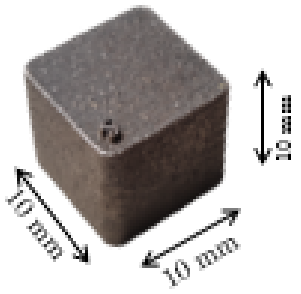


*Figure 10: dimensions of the cubic samples*

The software was used to input the predefined process parameters to each component. Each part was manufactured with a different combination of laser speed, laser power, and hatch spacing, resulting in characteristic features specific to that component. In addition, the samples were engraved with label identifiers during production that correspond to the sample IDs reported in table 5 to differentiate them based on their specific process parameters

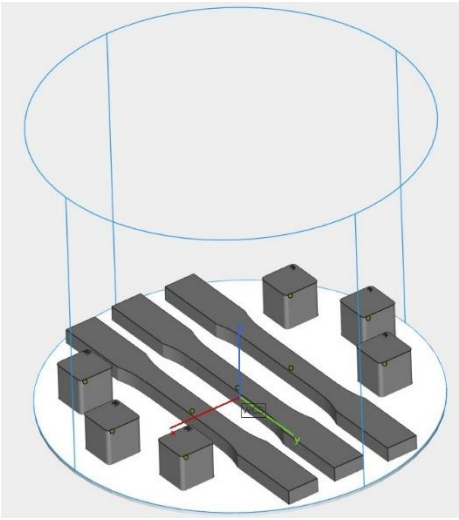

*Figure 11: CAD file of samples*

### 3.2.1. Design of Experiment

The Design of Experiments (DoE) for this study includes all the factors used at this experience. The experimental plan was organized into two main groups of factors:

1. the process parameters

2. the material composition.

On the process side, four controllable parameters were varied: layer thickness (L), laser power (P), laser scan speed (v), and hatch distance (h). [125] the specific levels reported in Table 5. These parameters and their ranges were selected from earlier studies with the machine and insights from previous studies, ensuring coverage of a processing window that minimizes the risk of lack-of-fusion defects at low energy input and excessive keyholing at high energy input. All other manufacturing conditions were keep constant to isolate the influence of these four variables and composition, including build orientation, scan strategy, shielding gas type, platform pre-heating, recoater settings, and environmental conditions.

*Table 8: Process parameters for each sample used in this thesis*

| **Process parameter** | **Standard** | **High** |
|---|---|---|
| laser power [W] | 180 | 200 |
| laser speed [mm/s] | 500 | 100 |
| Hatch distance [mm] | 0.01 | 0.01 |
| Layer thickness [mm] | 0.03 | 0.03 |
| VED [j/mm3] | 100 | 79 |

Three different compositions were printed in separate building jobs to assess the effect of h-BN on the stainless steel matrix:

1) AISI 316L,

2) AISI 316L with 0.1 wt% h-BN

3) AISI 316L with 0.3 wt% h-BN.

Powder preparation for each composition, as outlined in the Materials section, was completed prior to the printing stage. To ensure a fair and direct comparison, all builds were produced under identical process parameters and subjected to the same post-processing conditions. The fabricated specimens were subsequently evaluated according to a unified set of metrics, density or porosity, microstructure, and mechanical properties allowing the influence of processing conditions to be distinguished from the specific effects of BN reinforcement content

## 3.3. Sample Printing

The samples were produced using TruPrint 1000 by TRUMPF . This specific model is a metal additive manufacturing system based on Selective Laser Melting (SLM). It is specifically intended for the industrial manufacture of intricate components. This machine is well-suited for companies providing excellent precision and flexibility in materials, making it well-suited for applications where fine detail, compact microstructures, and fully functional prototypes are required.


*Figure 12: TruPrint 1000 by TRUMPF*

*Table 9: The technical features of the machine are documented in Table.*

| Category | Specification |
|---|---|
| Effective Build Volume (Standard) | Diameter 98 Mm X 100 Mm Heigh |
| Processable Raw Materials | Metal Powders for Welding in Powder Form, Such As Stainless Steels, Tool Steels and Aluminum, Nickel base, Cobalt-Chrome or Titanium Metal Alloys, Amorphous Metals. Current Availability of Materials and Their Parameters Available on Request. [1] Only with Optional Glove Box + High-Resolution Oxygen Sensor. |
| Maximum Laser Power at The Workpiece | 200 W |
| Beam Diameter (Standard) | 80 mm |
| Layer Thickness | 20 - 60 mm |
| Build Rate | 10 - 50 $Cm^3/h$ |
| **Connection And Consumption** | |
| Electrical Connection (Voltage) | 230 V |
| Electrical Connection (Current Intensity) | 7a |
| Electrical Connection (Current Intensity - Multilaser Option) | 9a |
| Electrical Connection (Frequency) | 50/60 Hz |
| Shielding Gas | Nitrogen, Argon |
| **Structural Design** | |
| Dimensions (W * H * D) | 780 mm * 2050 mm * 1160 mm |
| Weight (With Multilaser Option) | Max. 900 Kg |

A 3D model was created in CAD software, exported in STL or AMF format, sliced into layers using TRUMPF's Print software with a layer thickness of 30 µm, and with laser power, scan strategy, and

hatch spacing set, after which the build job file was generated and transferred to the TruPrint 1000 control system. During the final inspection, we verify that no corners of the sample overlap with the platform edges

The building chamber was first cleaned to ensure a contamination-free environment, after which the building platform was installed, leveled, and securely fixed. In the first job, stainless steel 316L of powder was loaded into the powder hopper. In the second job, the powder used was 316L with 0.1% BN, while in the third job, 316L with 0.3% BN was loaded. For all three jobs, high-purity argon gas was supplied to maintain an inert atmosphere within the construction chamber, thereby minimizing the likelihood of oxidation during the printing process.

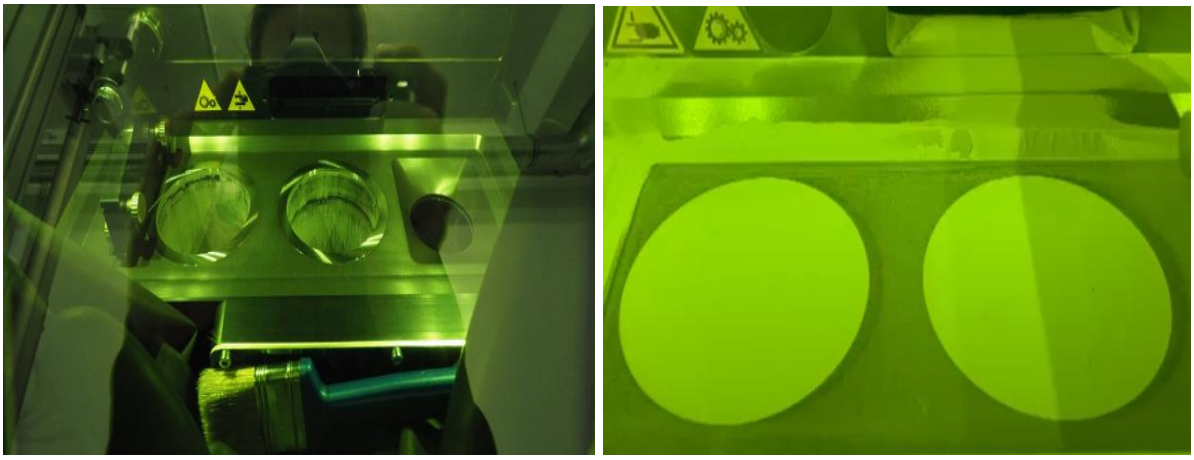

*Figure 13: TRUMPF machine setup before the start of the printing process, with the build platform installed*

The fabrication process was initiated from the machine's control panel, At the start of each cycle, the powder recoater distributed a thin, uniform layer of metal powder across the build plate, after which the fiber laser selectively melted the powder according to the sliced layer data. Once completion of a layer, the build plate was lowered by one layer thickness, and the process was repeated layer by layer until the entire part was fabricated.

A bidirectional stripe scanning pattern was employed with a 67° rotation between successive layers. This rotation strategy helped to reduce residual stress, minimize anisotropy, and enhance the mechanical properties of the printed parts. Each job requires almost three hours to complete the printing of samples, using a thick 30-micron layer.

On Figure 14, the highlighted region illustrates the laser in operation during the L-PBF process, where localized heating melts a thin layer of powder to form the desired geometry. The figure also shows the completed specimens still attached to the build platform after printing. Once fabrication

was finished, the chamber was cooled under an inert atmosphere to prevent oxidation. The build plate was then removed, and any loose powder was either brushed or vacuumed away, with the remaining material returned to the handling system for recycling.

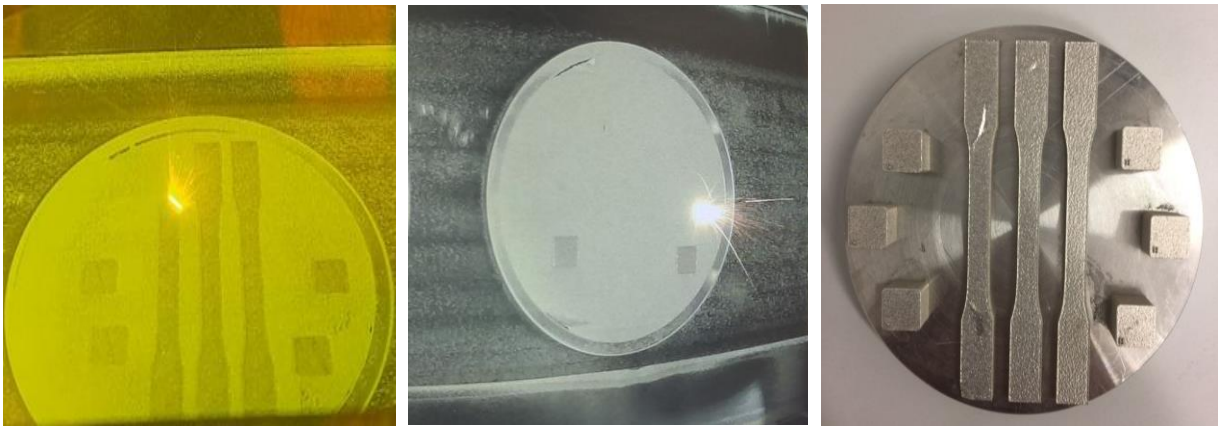

*Figure 14: (a)The platform during job running (b) samples after completion of 3D printing.*

## 3.4. Sample Characterization

During this stage, the fabricated samples were first detached from the build platform using wire electrical discharge machining (W-EDM), ensuring minimal material loss and preserving part integrity. Non-destructive evaluation was then performed using X-ray computed tomography (XCT) to assess surface morphology and detect potential defects. The density of the specimens was subsequently measured by the Archimedes method, followed by surface roughness testing to evaluate surface quality.

Comprehensive microstructural characterization was carried out through metallographic analysis, providing insights into internal porosity, defects, and overall structural integrity. Phase identification was conducted using X-ray diffraction (XRD), while optical microscopy (OM) offered complementary information on internal features. Scanning electron microscopy (SEM) was employed to examine grain morphology as well as the presence of solidification cracks and other microstructural defects. Finally, nanoindentation and wear tests were performed to evaluate the mechanical response of the material.

Together, this multi-step characterization approach provided a holistic understanding of the material properties and mechanical performance of the printed components.

.

### 3.4.1. Cutting Machine

Wire Electrical Discharge Machining (WEDM) is a non-contact process used to cut electrically conductive metals and alloys with high precision. It works by generating controlled spark discharges between a continuously moving wire electrode and the workpiece, both submerged in deionized water, which acts as a dielectric to cool the material, remove debris, and prevent unwanted arcing. The localized heat from the sparks melts and vaporizes small portions of the material, while the constant feeding of the wire ensures accuracy and prevents breakage, enabling the creation of intricate shapes and fine details.[126]

The "G.cut W-EDM" cutting machine was used to cut the samples at this precise stage, shown in Fig 15. The first image shows the software interface of the cutting machine, where parameters such as wire movement, automatic processing, and the start/stop functions are controlled. The second image presents the main section of the machine, where the workpiece is positioned and the cutting operation is performed.


*Figure 15: a) CAD Software of G.cut Machine b) G.cut W-EDM, coordinate display and cutting area*

The build platform was first secured to the wire-cutting machine using clamps. In the machine's positioning software, the wire was then aligned with the platform to establish the reference point for both the X and Y coordinates. After setting the correct alignment, the platform dimensions and orientation were loaded into the system, and the cutting process was begun. During operation, the wire moved continuously while high-frequency electrical pulses were generated between the wire and the workpiece. These discharges eroded the material in a controlled manner along the programmed cutting path, while dielectric fluid flushed the cutting zone to remove debris and ensure

process stability. Once the cut was completed, the machine automatically stopped, and the separated sample was removed from the fixture. Both the cut part and the remaining build plate were then cleaned to eliminate any residual dielectric fluid or particles. At the end of this stage, the printed samples were successfully detached and prepared for subsequent characterization procedures.

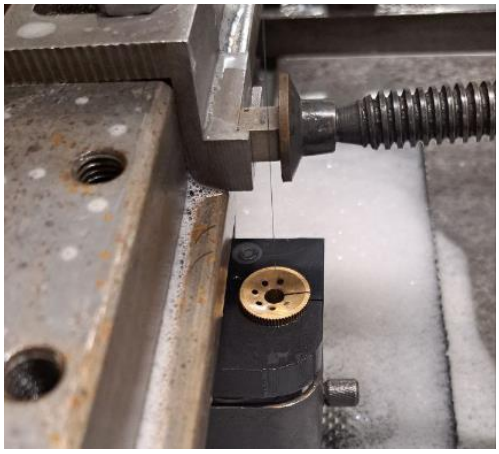

Figure 16. cutting the samples via Wire Electrical Discharge Machining

### 3.4.2. Archimedes Density

The Archimedes method was applied to determine the relative density of the components fabricated by SLM.[127] In this approach, each sample is weighed in two different media: first in air, which serves as the reference, and then in secondary fluid such as distilled water, acetone, or ethanol. Although distilled water is commonly used [128], it is not always suitable due to the tendency of air bubbles to form on the sample surface. This effect is particularly pronounced in lattice structures, where water's high surface tension can prevent complete infiltration into internal pores or meshes [129] To ensure accurate results, the Archimedes measurements were performed for each specimen using a Kern density balance, as illustrated in Figure 17, allowing both geometrical and Archimedes densities to be determined.

*Figure 17: a) Kern density balance and b)Set for density determination, c) Universal immersion basket for sinking and floating solid matter*

The Archimedes density measurement method is done accordance to the ASTM F3637-23, was employed to calculate the total porosity of the samples.

For this procedure, the measurement chamber was first prepared by filling the beaker with distilled water (density 0.997 g/cm³). The balance was calibrated, and the dry weight of the sample ($w_{dry}$) was recorded, as shown in Figure. The device was then reset to zero, and the sample was fully immersed in distilled water using the immersion basket, suitable for both sinking and floating materials. During immersion, air bubbles were carefully removed to avoid measurement errors, and the immersed weight ($w_{immersion}$) was recorded. Immediately after removal from the water, the sample was reweighed in air to determine the wet weight ($w_{wet}$), reflecting the amount of water absorbed during immersion. Each weighing step was performed three times, with the mean value taken for subsequent porosity calculations.

The theoretical density of the reference AISI 316L was determined by the relative method to be 7.987 g/cm³. For BN-reinforced samples, the theoretical density decreased slightly with increasing reinforcement content, measured as 7.97 g/cm³ for 0.1 wt.% BN and 7.92 g/cm³ for 0.3 wt.% BN.

Subsequently, the total porosity percentage and relative density percentage for all samples were computed utilizing the given formulas.[130]

$Archimides\ density\ (apparent\ density)$: $[\frac{g}{cm^3}]$

$$\rho_{Archimedes} = \rho_{liquid} \times \frac{w_{dry}}{w_{dry} - w_{immersion}}$$

$Geometrical density (bulk density)$: [$\frac{g}{cm^3}$]

$$\rho_{Geometrical} = \rho_{liquid} \times \frac{w_{dry}}{w_{wet} - w_{immersion}}$$

$where$:

Total porosity percentage = $\frac{\rho_{teorethical} - \rho_{bulk}}{\rho_{theoretical}} \times 100\%$

Relative Density percentage = $\frac{\rho_{Archimedes}}{\rho_{theoretical}} \times 100\%$

### 3.4.3. Roughness Test

Surface roughness was evaluated using a contact profilometer (RTP80-TL90, Someco SM SRL, Italy), as shown in Figure 19, to characterize the surface texture of the fabricated parts. The instrument operates by moving a precision stylus across the sample surface, detecting vertical height variations and generating a detailed surface topography profile. Measurements were taken on the build surface (the plane perpendicular to the build direction) to assess the finish quality of the printed components. Key roughness parameters were extracted, including Ra (arithmetic mean roughness), Rz (maximum profile height), and Rt (total height variation), which together provide an indication of manufacturing quality and surface integrity. While Ra is the most commonly reported parameter in additive manufacturing studies, it provides only limited insight since it does not account for wavelength variations. In contrast, Rz often shows a stronger correlation with tactile and visual impressions of surface quality. while it should be noted that surface texture and even material color can influence perception, meaning that Rz alone cannot fully capture all surface quality differences.[131], [132]


*Figure 18: profilometer (RTP80-TL90)*

Surface roughness measurements were performed on the top surface of the samples, with the profilometer scanning direction oriented perpendicular to the laser scan traces. Each specimen was securely mounted in the holder, and the stylus position was carefully verified to ensure proper contact with the surface and alignment orthogonal to the scan lines. The system was then calibrated, and the measurement parameters were configured according to standard surface metrology guidelines: a cut-off length of 0.8 mm, five cut-off numbers, and a scanning speed of 0.5 mm/s.

*Figure 19: measuring setup of sample*

The acquired measurement data and corresponding profile charts were saved in PDF format within the designated directory and later analyzed as part of the Results and Discussion section.

### 3.4.5. Metallography

Metallography is the study of the microstructure of metals and alloys using techniques such as optical and electron microscopy. It requires careful sample preparation, typically involving sectioning, mounting, grinding, polishing, etching to reveal the internal structure. This analysis helps in understanding valuable features like grain size, phase distribution, porosity, and defects, all of which critically influence mechanical properties including strength, hardness, and toughness. Clear and reliable observations depend heavily on proper preparation procedures.

The process of grinding and polishing was performed using a Presi machine, as seen in Fig 21. This is done using abrasive papers with increasing fineness of grit, typically ranging from coarse. At first, abrasive SiC papers with grit sizes of P320, P600, P800, P1200, and P2400 were chosen for grinding as can be seen in Fig 21 .

*Figure 20: The Presi machine was used for the grinding and polishing of the samples. And SiC abrasive papers*

The grinding process began with the coarsest abrasive paper (P320), which was first moistened before being mounted on the machine. The machine was then operated at a rotational speed of 150–200 rpm. Water was continuously supplied during grinding to remove abraded particles and to prevent overheating of the sample. Each specimen was placed on the abrasive paper and ground in a manner that produced uniform, parallel lines in a single direction. After approximately 3–4 minutes of grinding with each paper, the surface was examined under a microscope to verify the presence and clarity of the grinding lines. Once confirmed, the specimen was rotated by 90° and the next finer grit paper was applied to remove the previous set of lines and produce a new pattern. This sequence

was repeated progressively with finer abrasive papers until the final stage was reached using P2400 grit.

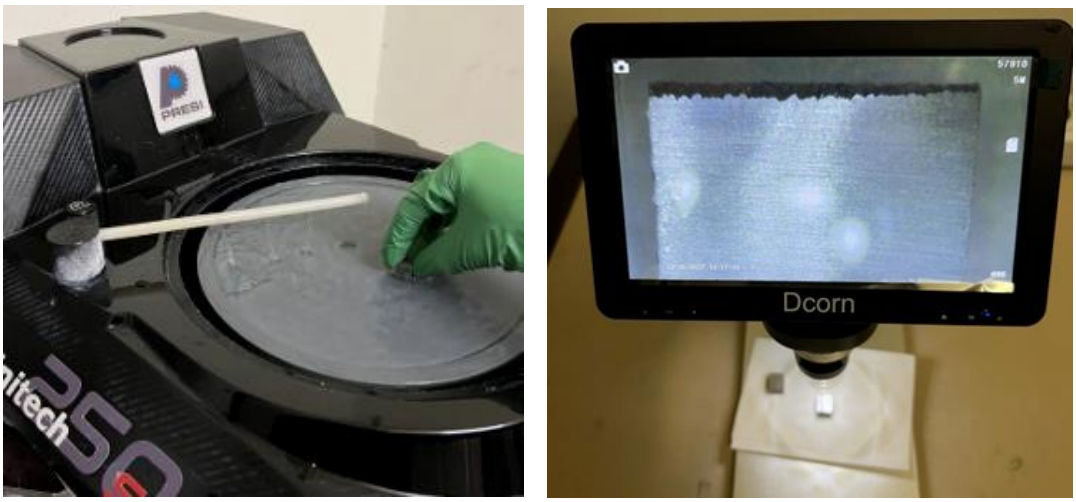


*Figure 21: microscope for assessing the visibility of the grinding lines*

Following the grinding stage, the samples were polished to remove residual scratches and obtain a mirror-like surface suitable for microstructural analysis. Polishing was done in two successive steps, using pads with grit sizes of 3 µm and 1 µm, while the rotational speed was reduced to 50–80 rpm. During polishing, the specimens were gently moved back and forth across the pad to ensure a uniform finish. In the first step, a 3 µm diamond stick was applied to a blue polishing pad, together with a lubricant to minimize friction and prevent the introduction of new scratches. The surface was then further refined using a 1 µm diamond suspension on a pink polishing pad, achieving the desired smoothness, as shown in Fig. 23.

*Figure 22: the pink and blue pads 3 and 1 µ pads . a) 3µ Diamond paste used during the polishing process with the blue pad. b) Diamond suspension used on pink pad*

After this phase, the surfaces of the sample were supposed to be very smooth and reflective, such as a mirror. The samples were now prepared for the subsequent phase, in which the microstructure was analyzed using an optical microscope at 50X magnification for porosity analysis.

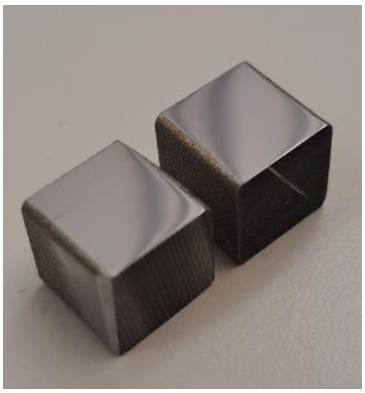

*Figure 23: Pictures of mirror face of samples.*

To investigate the austenite microstructure of the samples and examine the grain size , grain boundaries and melt pool created under different compositions, polished samples underwent etching. The etching procedure employed 100 mL of Aqua regia, as demonstrated in Fig 24, It is typically prepared by mixing concentrated nitric acid ($HNO_3$) and concentrated hydrochloric acid (HCl) in a 1:3 volume ratio. Formula of etchant:

$$HNO3+3HCl \rightarrow NOCl+Cl2+2H2O$$

Initially, the samples were submerged in the solution for 8 seconds. They were then rinsed with water to eliminate any residual etchant, and the surfaces were dried with dryer. The samples were subsequently analyzed using an optical microscope to observe the grains boundaries and defects.

*Figure 24: aqua regia etchant*

## 3.5. Microstructures Analysis

The microstructural features of the fabricated specimens were examined through a multi-technique approach, using X-ray computed tomography (XCT), optical microscopy, X-ray diffraction (XRD), Optical Microscopy (OM), scanning electron microscopy (SEM), and these complementary techniques were employed to examine surface morphology, internal features, and phase composition of the fabricated specimens. The specific procedures and parameters for each method are described in the following sections.

### 3.5.1. X-ray Computed Tomography

X-ray computed tomography (XCT) has become an increasingly important tool for non-destructive inspection. The technique produces a three-dimensional (3D) reconstruction of an object by combining a series of two-dimensional (2D) X-ray images taken from multiple angles The principle is based on the differential absorption of X-rays by the material: denser regions absorb more X-rays, while less dense regions allow more X-rays to pass through. These varying absorption levels are recorded by a detector as projection images. Specialized reconstruction algorithms, such as filtered back projection or iterative reconstruction, then process these images to generate a volumetric dataset that reveals the object's internal structure without physically altering or damaging it[133] For composite materials, XCT offers distinct advantages: their inherent heterogeneity and complex architecture often require 3D characterization, and the ability to monitor the nucleation and progression of defects is vital for assessing structural integrity.[134].

XCT was performed using the "Phoenix v|tome|x S system" as in Figure that system is a versatile, high-resolution system used for 2D X-ray inspection, 3D computed tomography (micro-CT and nano CT), and 3D metrology. It is suitable for various non-destructive testing (NDT) applications and materials analysis. The system offering up to twice the scanning speed and doubled resolution for

smaller assets, and uniquely combining Dynamic 41 detector technology with a High-flux|target to deliver faster scans or improved accuracy, thereby revolutionizing inspection capabilities.


*Figure 25: Phoenix v|tome|x S XCT system*

One sample representative from each composition was selected for XCT analysis. The objective was to determine porosity percentage and density, with the results subsequently compared to those obtained by alternative measurement techniques. Each specimen was mounted on the holder, as illustrated in Figure 31. To minimize beam-hardening effects and enhance image contrast, a 0.5 mm Sn filter was placed in front of the X-ray source. The sample position was then verified and adjusted using the system software to ensure accurate alignment within the imaging frame. Once the setup was confirmed, the tomographic scan was initiated.

Comprehensive data were obtained on porosity distribution, pore geometry, pore size (diameters), and other relevant characteristics, which will be further elaborated in the result section.

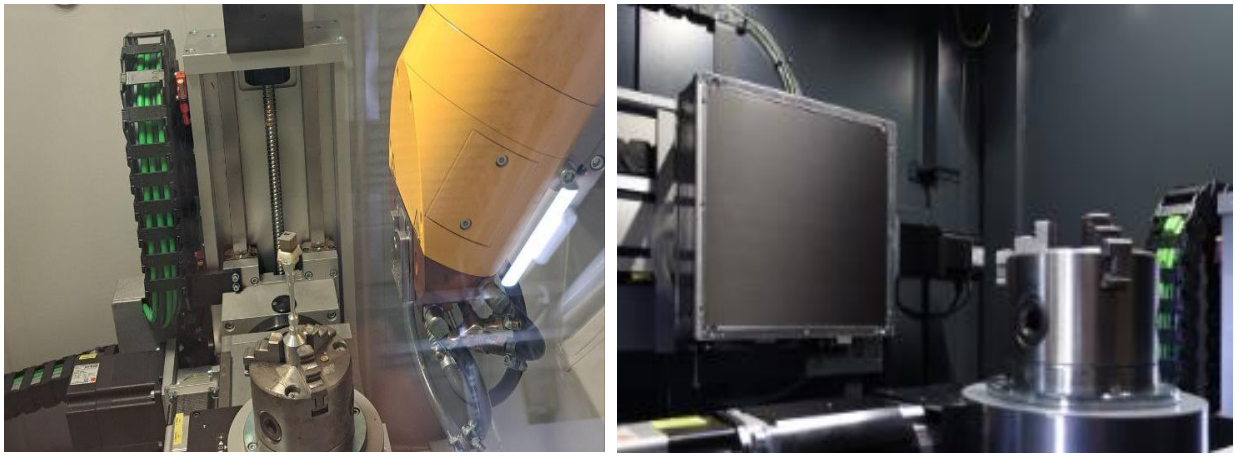

*Figure 26: a) X-ray beam gun and sample holder for tomography analysis. b) Detector configuration for accurate tomography analysis.*

In XCT analysis, Phoenix datos|x software is used primarily for the 3D reconstruction of raw projection data acquired during scanning. It transforms multiple 2D radiographic images into a volumetric dataset using reconstruction algorithms, while also applying corrections like beam-hardening adjustment to minimize artifacts from uneven X-ray absorption. These corrections enhance image contrast and render the material structure more uniform. The reconstructed data is then processed in VGStudio MAX, which provides advanced tools for visualization and quantitative analysis. This includes feature segmentation, refinement of over-segmentation, differentiation between solid regions and voids or porosity, and precise measurement of internal structures. The software also enables the generation of high-quality visualizations and cross-sectional views to support interpretation and reporting.

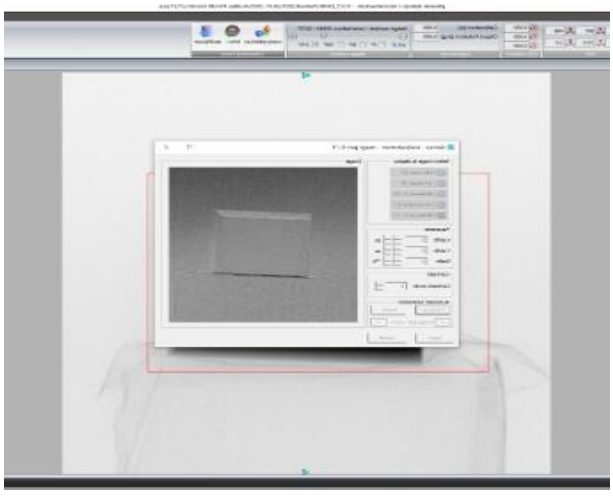

*Figure 27: a) "Phoenix datos|x" software for 3D reconstruction of the XCT data. .*

### 3.5.2. X-ray Diffraction

X-ray diffraction (XRD) is an analytical technique used to identify and characterize the crystalline phases present in a material and to obtain information about its crystallographic structure, lattice parameters, and grain size. The technique requires homogeneous and crystalized structure of samples; besides it has the limitation of peak overlay that may occur and worsen high angle. XRD is performed to determine the phase composition, crystal structure, crystallite size, strain, and preferred orientation (texture) of materials. It is essential in fields such as metallurgy, as it enables researchers to verify material identity, assess purity, detect phase transformations, and correlate microstructural characteristics with material properties[135].

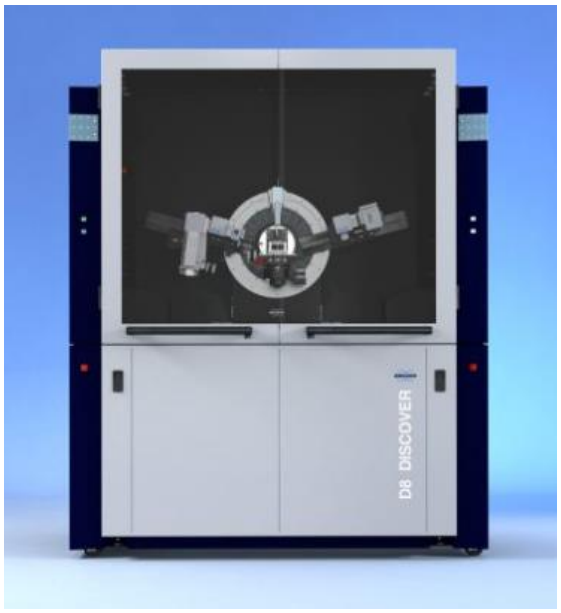


*Figure 28: D8 DISCOVER - XRD machin*

X-ray diffraction (XRD) analysis was performed to identify the crystalline phases present in the fabricated specimens and to evaluate possible phase transformations induced during processing. The technique relies on the constructive interference of monochromatic X-rays diffracted by the periodic atomic planes of the crystal lattice, providing characteristic diffraction patterns for each phase. By analyzing the diffraction peaks in terms of their position, intensity, and width, information about lattice parameters, crystallite size, and residual stresses can be obtained. In this study, XRD was employed to confirm the phase constitution of the 316L stainless steel matrix and to detect any secondary phases or reinforcements formed because of the additive manufacturing process and subsequent thermal cycles

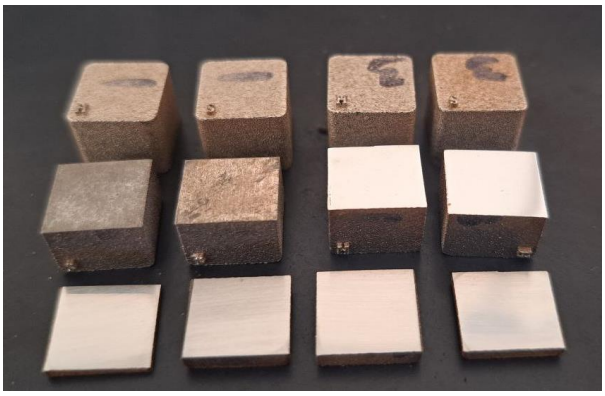

*Figure 29: prepared samples to XRD test*

### 3.5.3. Optical Microscope

After polishing, the sample surfaces were examined using an optical microscope. A Leica DM6 optical microscope (Fig. 31) equipped with a manual X–Y stage and objectives offering magnifications from 5× to 100× was used for this analysis. The system was coupled with LAS X software, which enabled advanced image acquisition and processing.

*Figure 30: Optical Microscope DM6 by Leica*

The samples were carefully placed on the microscope stage with the surface of interest facing downward, making sure that their build direction was correctly aligned. The surfaces were then

examined at different magnifications to capture both general and detailed views of the area. By gently adjusting the stage knobs, a series of overlapping images was taken to cover the entire surface.

For each image, the focus was precisely adjusted to achieve the best clarity, which was especially important for observing small pores and fine details. This approach provided images at varying levels of detail, allowing both a broad overview and a closer look at specific surface features.

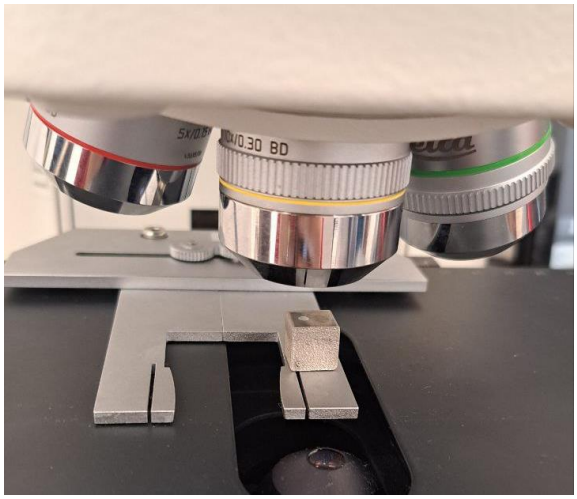


*Figure 31: The sample is placed in a down position for analysis using an optical microscope.*

### 6.5.4. Scanning Electron Microscopy

Scanning electron microscopy (SEM) is a high-resolution imaging technique that uses a focused beam of high-energy electrons to scan the surface of a specimen. As the electrons interact with the atoms of the sample, several signals are generated, including secondary electrons, which are used to form detailed images of surface morphology. The technique provides topographical, compositional, and, in some cases, crystallographic information at the microscale. [136]

Scanning electron microscopy with energy dispersive X-ray spectroscopy (EDX) has been designed to examine chemical composition. SEM and EDX provide simple, non-destructive and rapid measurements in a wide range of matrices[137]. EDS often integrated with SEM, is used to analyze the elemental composition of a material. When the electron beam strikes the sample, it can eject inner-shell electrons, leading to the emission of characteristic X-rays. These X-rays are then detected and analyzed to identify and quantify the elements present in the sample.[138]

The samples were examined by SEM using a JEOL JCM-6000Plus (Figure 33) operated at 5 kV accelerating voltage. Micrographs at multiple magnifications were acquired to evaluate surface microstructure and defects.


*Figure 32: Versatile Benchtop SEM JEOL JCM-6000Plus*

Once the specimen was prepared, the SEM chamber was vented, and the sample stub was securely placed on the stage, ensuring the correct orientation and proper clamping. The stage height (Z-axis) was adjusted to a safe position, confirming sufficient clearance for any planned tilt or rotation during imaging. The chamber was then evacuated to the required vacuum level, monitoring for signs of outgassing that could indicate contamination or the presence of volatile materials. After achieving a stable vacuum, the appropriate detector was selected based on the imaging objective: the secondary electron (SE) detector was used to obtain high-contrast surface and topographical details, while the backscattered electron (BSE) detector was employed to highlight compositional differences and provide flatter topography.

### 3.5.3. Image Analysis

After image acquisition, the micrographs were processed and analyzed using **ImageJ** software ImageJ, originally developed by the U.S. National Institutes of Health, is a Java-based program

widely used for image analysis in scientific research. In this study, it was employed to quantify the porosity percentage, evaluate crack density, and perform grain size analysis of the polished samples.

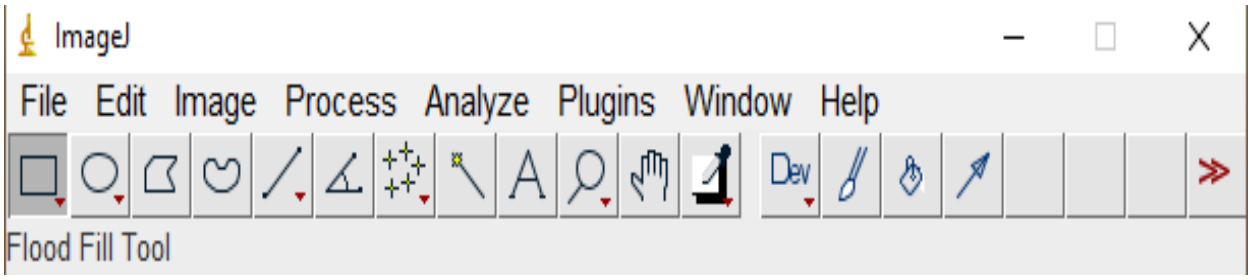


*Figure 33: ImageJ software*

Since ImageJ requires 8-bit images, the first step in the analysis was to convert the micrographs into 8-bit format, producing grayscale representations in which each pixel intensity corresponded to the local gray level. This conversion facilitated quantitative evaluation of pore and crack density across the surfaces. By carefully adjusting the threshold settings, distortions arising from polishing artifacts or residual scratches were minimized. As a result, the program was able to accurately identify and quantify the dark regions associated with pores and cracks, enabling precise measurement of their percentage in the samples.

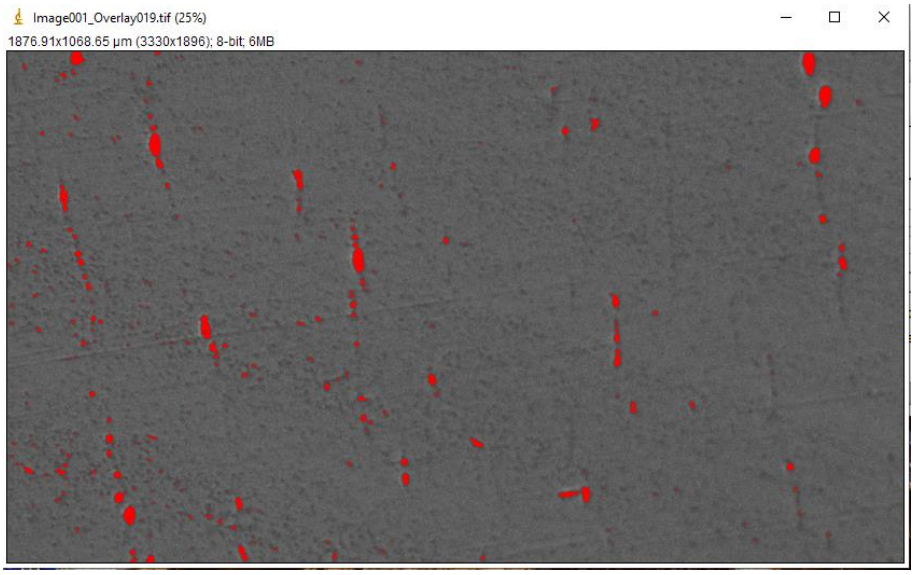


*Figure 34: The thresholded image, where pores/cracks are highlighted in red*

## 3.6. Mechanical Tests

The mechanical behavior of the printed samples was evaluated using two complementary methods: nanoindentation and wear testing. Nanoindentation allowed us to probe the hardness and elastic modulus at the sub-micron scale, giving a detailed view of how the material and BN reinforcement respond to localized loading. In contrast, wear testing focused on the practical performance of the samples under sliding conditions, measuring weight loss and resistance to wear. By combining these approaches, we were able to capture both the fundamental mechanical properties and the real-world durability of the material. The procedures for each test are described in the following sections

### 3.6.1. Nano indentation

Nanoindentation is an effective technique for evaluating the deformation mechanisms of materials at the sub-micron scale, providing insights into indentation modulus, hardness, strain-rate sensitivity, and creep behavior of L-PBF AISI 316L fabricated parts[139], [140]However, there is limited literature linking these mechanical properties to specific microstructural regions, which is essential for interpreting anisotropy in surface mechanics as well as variations across different grain morphologies, microstructural features, and crystallographic orientations [141]

The polished samples were prepared for nanoindentation testing using the Hysitron TI 950 TriboIndenter, as shown in Figured 36. To evaluate the mechanical properties of the samples at the microscale. This is a high-precision instrument designed for nano indentation and related nanomechanical testing. It features advanced feedback control for enhanced testing precision, a dual-head configuration enabling both nano- and microscale measurements, and exceptional noise floor performance. The TI 950 is capable of measuring properties such as hardness, elastic modulus, creep, and fracture toughness at the nanoscale. It can also perform scratch testing, wear testing, and modulus mapping with extremely high resolution in both force and displacement.

*Figure 35: Hysitron TI 950 TriboIndenter*

For nanoindentation testing, the samples were first sectioned using EDM to minimize thermal effects, undesired phase transformations, and residual stresses, thereby preserving both the microstructure and micromechanical properties. The specimens were then carefully ground and polished to achieve a smooth, scratch-free surface suitable for indentation. A prescribed displacement depth was applied, and nine indents were performed across three distinct regions of each sample, with a minimum of 20 repetitions for each testing condition. To prevent overlap of plastic deformation zones, a spacing of 10 μm was maintained between adjacent indents.

The instrument was equipped with a three-plate capacitive transducer, enabling high-precision measurement of load and displacement, which allowed the calculation of hardness and elastic modulus from the resulting load–displacement curves. A Berkovich diamond indenter tip, featuring a three-sided pyramidal geometry, was employed due to its established suitability for characterizing metallic and composite materials. Prior to testing, the system was calibrated using a fused quartz reference standard to ensure the accuracy of both load and displacement measurements.

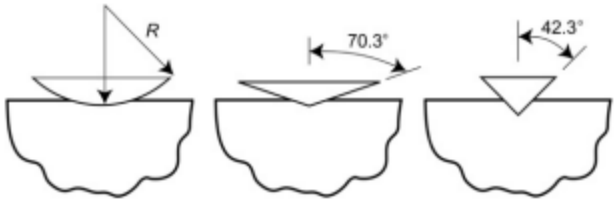


For each sample, 9 indents were performed at different regions to account for microstructural heterogeneity and improve statistical reliability. The Oliver and Pharr method was used to extract hardness (H) and reduced elastic modulus (Er) from the load–displacement curves.[142]

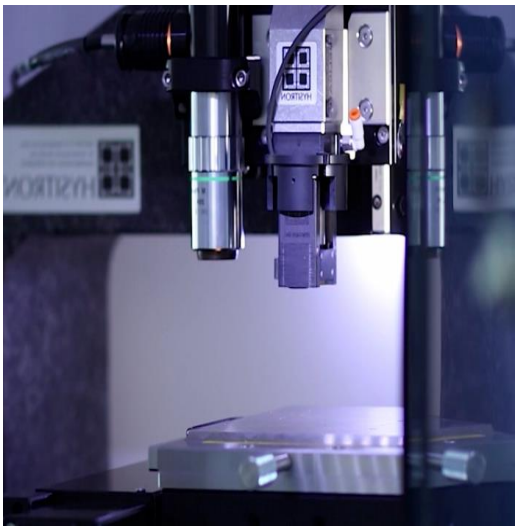

*Figure 36: place of sample in machin*

According to Oliver-Pharr method, the hardness (H) and reduced elastic modulus (Er) calculated from the load-displacement curves: [143]

$$\boldsymbol{H} = \frac{\mathrm{Pmax}}{\boldsymbol{Ac}}$$

Where:

Pmax: Maximum applied load [μN]

Ac: Contact area at maximum load

And Ac calculated from contact depth hc and the indenter geometry that for a Berkovich indenter is: [143], [144]

$$A_c = 24.5h_{c2}$$

Reduced Elastic Modulus (Er):

$$E_r = \frac{\sqrt{\pi}}{2\beta} \times \frac{S}{\sqrt{Ac}}$$

S = Contact stiffness $[\frac{mN}{nm}]$

β = Correction factor for indenter geometry (for Berkovich tip ~1.034).

For Young's Modulus of the Sample (E),

The reduced modulus $E_r$ accounts for both sample and indenter deformation. To obtain the true elastic modulus of the sample (E):

$$\frac{1}{Er} = \frac{1-\nu^2}{E} + \frac{1-\nu i^2}{Ei}$$

Where:

ν: Poisson's ratio of the sample.

Ei : Elastic modulus of indentor

νi =Poisson's ratio of the indenter

(for diamond: Ei=1140 GPa, νi=0.07 Ei = 1140)

From the nanoindentation results, the hardness and modulus were combined to give an idea of how well the material can resist wear. Two common indicators are used: the $H/E_r$ ratio, which shows how much elastic strain the material can handle before failure, and $H^3/E_r^2$, which points to how resistant it is against plastic deformation. In simple terms, a higher $H/E_r$ value (above about 0.1) means the material is more elastic and less likely to crack, while a higher $H^3/E_r^2$ value suggests it can better withstand abrasive wear.[145]

### 3.6.2. WearTest

Wear resistance of the fabricated samples was evaluated using a reciprocating wear test under controlled laboratory conditions. The test was performed on three specimens; each prepared with dimensions and surface suitable for the tribological setup.

A constant normal load of 10 N was applied to the specimens during the test. The sliding motion was carried out at a frequency of 1200 cycles per minute, corresponding to a linear sliding speed of approximately 880 mm/s. The tests were conducted at ambient room temperature to simulate standard service conditions. A zirconia counter-body ball was employed as the counterpart material, selected for its high hardness and stability to ensure reproducible wear tracks.

The wear test was run for a fixed time duration, after which the mass loss of each specimen was recorded with a high-precision microbalance. In addition, the coefficient of friction (CoF) was continuously monitored and recorded throughout the test using the system's integrated data acquisition unit.

The mass loss of each specimen is determined by measuring its weight before and after the wear test, with the difference representing the material removed during sliding

$$V=\frac{\Delta m}{\rho}$$

$\Delta m = m_{initial} - m_{final}$.

Calculate specific wear rate Ws to normalize by load and sliding distance:

$$W_s= \frac{V}{F.L}$$

where:

V = volume loss [mm³]

F = applied load [N]

L = total sliding distance [m]

# 4. Result and Dissection

## 4.1. Overview

The Selective Laser Melting (SLM) process is influenced by a wide range of variables, which makes it necessary to establish a rigorous framework that both improves the mechanical properties of the fabricated parts and reduces defects and porosity. To achieve this, it is important to adopt a clear and systematic approach. The objective of this thesis is to develop and apply such a method to address both requirements. Based on the existing literature, a specific research plan was designed and implemented to accomplish this goal.

According to this roadmap, within this framework, a series of cubic specimens were fabricated by incorporating different amounts of BN reinforcement while applying optimized processing parameters. These tests helped to find the best combinations of parameters and material composition for improving the mechanical properties. The analysis of the samples produced a set of data, which is presented in this chapter with numbers, graphs, and discussion.

The structure of the chapter is outlined as follows:

a) Powder Analysis: Presents scanning electron microscopy (SEM) images of the starting powders, highlighting particle morphology, size distribution, and surface features that influence powder flowability and melting behavior.

b) Surface Quality Evaluation: Analyzes the effect of processing conditions on the rough surface of the manufactured components, assessing the trade-off between parameter selection and final part quality.

c) Microstructural Characterization: Examines the influence of BN reinforcement on the microstructure, focusing on matrix integrity, grain morphology, and the distribution of reinforcement phases.

d) Mechanical Performance Testing: Evaluates the mechanical response of the samples through compression testing, with emphasis on correlating material quality to process efficiency and defect formation.

## 4.2. Powder Analysis

Gas-atomized AISI 316L shows predominantly spherical particles (typical D10–D90 ≈ 10–63 μm) with occasional satellites, with smooth particle surfaces and only a few attached satellites.

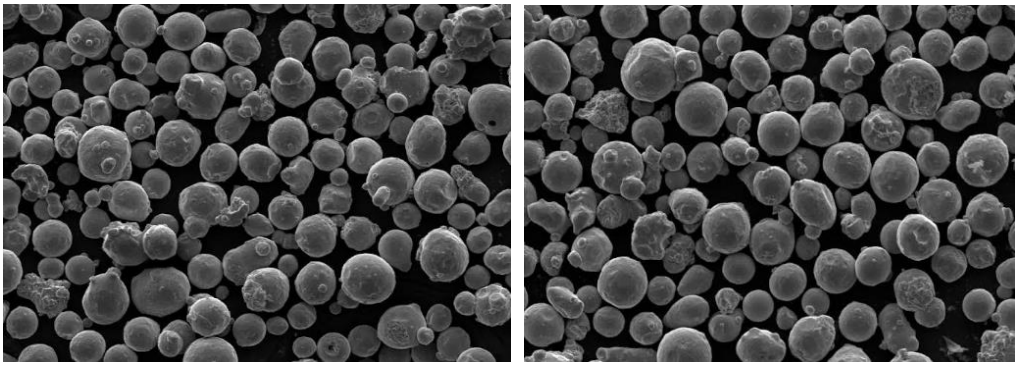

*Figure 37: SEM of Gas-atomized AISI 316L powder*

Figure 37 shows the SEM images of the feedstock powder obtained by blending gas-atomized 316L stainless steel with BN reinforcement. At low magnification, the powder bed is dominated by nearly spherical 316L particles with a relatively narrow size distribution, confirming the typical morphology of atomized powders, which ensures good flowability and packing behavior during the SLM process. At higher magnification, the presence of BN reinforcement can be observed. BN appears as smaller, angular, and plate-like particles that are distributed over the surfaces of the spherical 316L particles. Some local agglomerates of BN are also visible, suggesting partial clustering during mixing. The adhesion of BN onto the stainless steel powder surface is beneficial for ensuring the delivery of reinforcement into the melt pool, although inhomogeneous distribution or clustering may influence melt pool stability and porosity formation. Overall, the SEM analysis confirms a generally homogeneous mixture, where spherical 316L particles provide good base morphology for powder spreading, while BN is effectively incorporated as a secondary phase adhered to the particle surfaces.

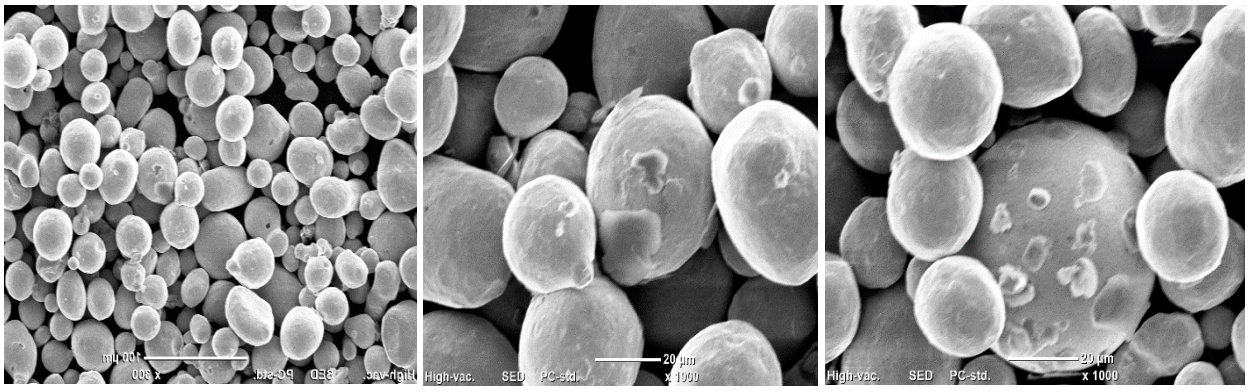


*Figure 38: micrographs of the BN–316L blended powder: a) low-magnification overview showing spherical morphology of 316L particles; b,c) higher-magnification views highlighting BN powder distributed on the surfaces of 316L particles and occasional BN agglomerates.*

In the 0.3 wt% BN–316L mixture, the spherical morphology of the 316L base powder is still preserved; however, the amount of BN decorating the particle surfaces is visibly higher compared to the 0.1 wt% blend. BN platelets appear more frequently, and local agglomerates are clearly observed at higher magnification. Such clusters may compromise the uniformity of powder spreading, induce inter-particle bridging, and disturb melt-pool wetting and solidification during the SLM process.

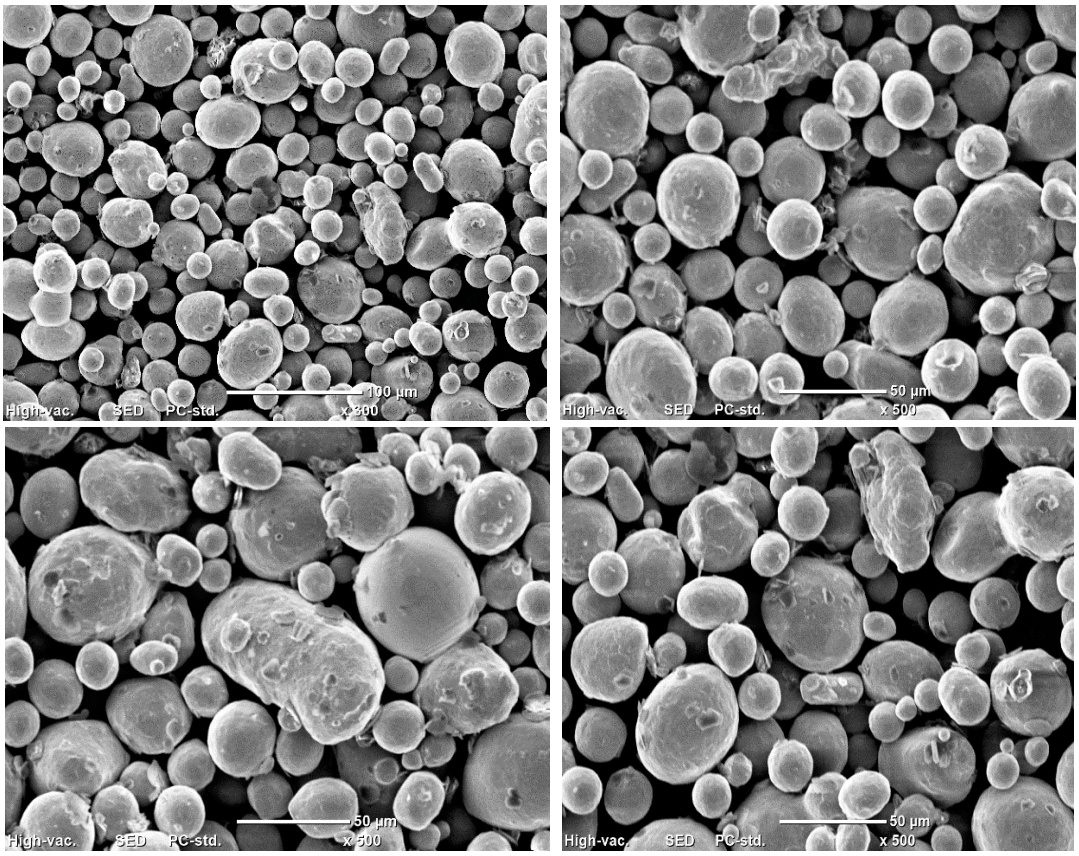


*Figure 39: SEM micrographs of the 0.3 wt% BN–316L blended powder. b-d) highlighting BN distribution and local agglomeration at various locations.*

When comparing the blended powders, the 0.1 wt% BN–316L mixture shows BN platelets sparsely distributed on the surfaces of the spherical 316L particles, with good overall dispersion and only limited signs of clustering. In contrast, the 0.3 wt% BN–316L mixture exhibits a higher number of BN particles and more frequent local agglomeration. While the spherical morphology of the 316L base powder ensures generally good flowability in both cases, the increased BN content at 0.3 wt% reduces dispersion uniformity and may locally disrupt powder packing and layer homogeneity during the SLM process.

The X-ray diffraction (XRD) analysis was performed on the 316L stainless steel powder, the pure h-BN powder, and their mixtures containing 0.1 and 0.3 wt% h-BN. The diffraction pattern of 316L

revealed the main reflections of austenitic stainless steel, confirming the presence of its single-phase face-centered cubic (FCC) structure without detectable secondary phases. The h-BN powder, on the other hand, exhibited its characteristic peaks associated with the hexagonal structure.

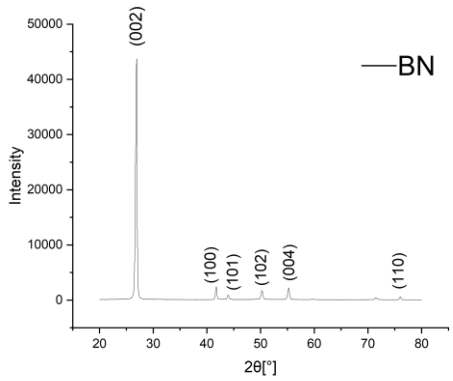


*Figure 40: XRD analysis and peaks of the AISI 316 L and pure h-BN*

In the blended mixtures, the diffraction profiles were dominated by the strong peaks of 316L; however, additional weaker peaks corresponding to the h-BN phase were also visible. The intensity of these peaks increased slightly with higher h-BN content, providing clear evidence of its presence within the composite powders. These observations confirm that the h-BN particles were not dissolved into the steel matrix during blending but instead retained their crystalline identity and were successfully incorporated into the stainless steel powder system.

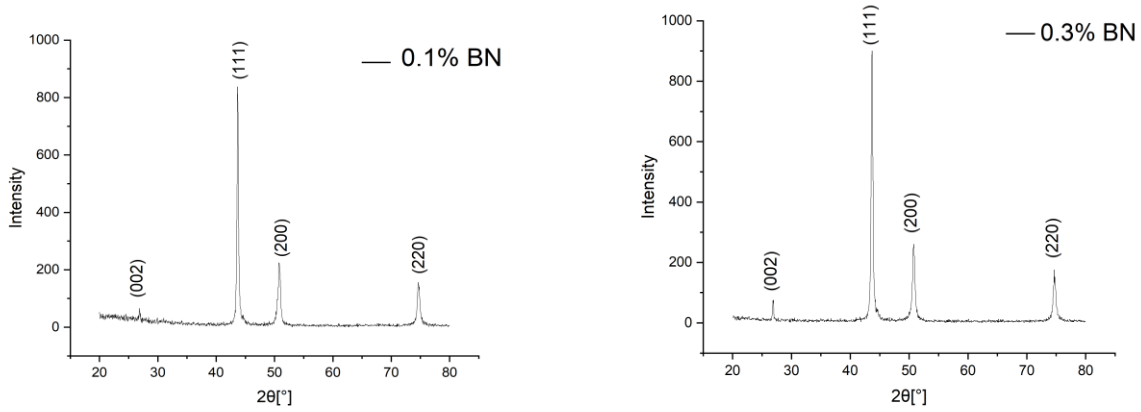


*Figure 41: XRD analysis of the blended mixture powders*

### 4.3. Surface Quality Evaluation

The profilometer was operated with a cut-off length of 0.8 mm, a cut-off number of 5, and a scanning speed of 0.5 mm/s, in accordance with standard surface metrology guidelines. Surface roughness measurements of the top surfaces of the as-built specimens were repeated three times, and the average values with standard deviations are reported in Table 10. Both the arithmetic mean roughness (Ra) and the average peak-to-valley height (Rz) were measured for samples produced with standard (S) and high (H) laser scanning speeds in different compositions.

*Table 10: Surface roughness (Ra and Rz) of the top surfaces of as-built 316L and BN–316L specimens produced with standard (S) and high-speed (H) laser scanning.*

| Sample | | Ra (µm) | Rz (µm) |
|---|---|---|---|
| **316L** | S | 7.37 ± 0.34 | 38.83 ± 1.7 |
| | H | 6.85 ± 0.36 | 37.06 ± 1.9 |
| **0.1% BN–316L** | S | 6.83 ± 0.31 | 39.74 ± 1.75 |
| | H | 6.69 ± 0.33 | 38.69 ± 1.95 |
| **0.3% BN–316L** | S | 7.01 ± 0.36 | 40.04 ± 1.82 |
| | H | 6.84 ± 037 | 37.97 ± 1.94 |

For the reference 316L sample, Ra values of 7.37 µm (standard speed) and 6.85 µm (high speed) were obtained, with corresponding Rz values of 38.83 µm and 37.06 µm. The addition of 0.1 wt% BN slightly reduced the average roughness, yielding Ra values of 6.83 µm (standard) and 6.69 µm (high speed). In contrast, the 0.3 wt% BN–316L sample exhibited Ra values of 7.01 µm (standard) and 6.84 µm (high speed), which are comparable to those of the undoped 316L alloy.


**AISI 316 L - H**


**AISI 316 L – S**

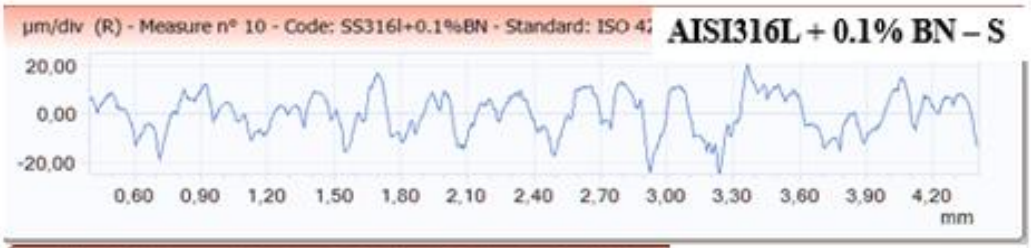


**AISI316L + 0.1% BN – S**


**AISI 316L + 0.3 % BN- H**


**AISI316L + 0.1% BN – H**


**AISI 316L + 0.3 % BN- S**

Overall, the limited variation in roughness across compositions can be attributed to the low BN content (≤0.3 wt%), which is insufficient to significantly alter the melt pool dynamics that primarily determine surface topography. In L-PBF, surface roughness is largely influenced by processing parameters such as laser power, scan speed, hatch spacing and particle adhesion, rather than minor compositional changes. Thus, while BN addition affected microstructural and mechanical properties, its impact on the top surface roughness remained negligible.

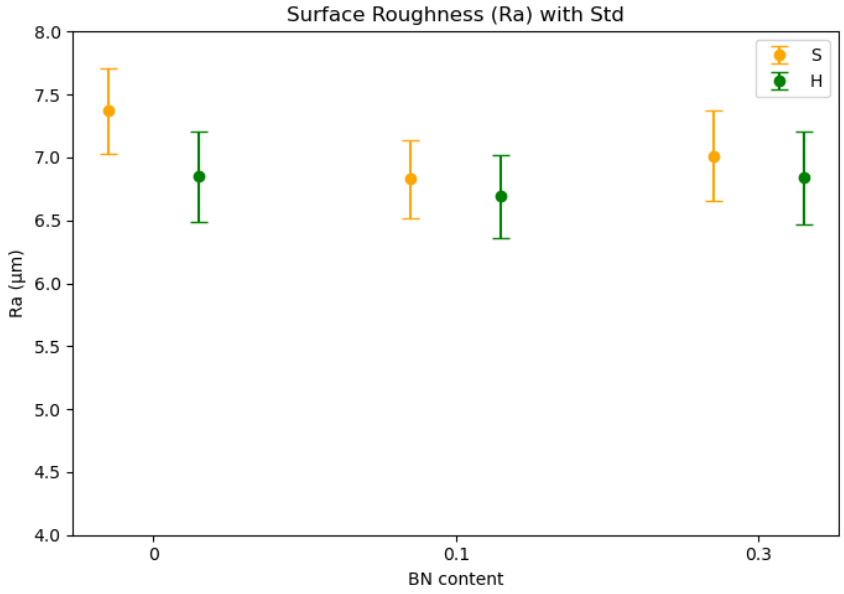


*Figure 42: Surface roughness of samples based on BN content*

## 4.4. Microstructure Analysis

This section presents the results obtained from the measurement techniques described in the previous chapter. The key data analyzed in this thesis concerns the relative density of the samples, determined using three different approaches: X-ray computed tomography (XCT) and Archimedes' method, image-based analysis.

The relative density of the samples was first evaluated using Archimedes' method. This approach provides a bulk estimation of density, accounting for both open and closed pores, and is widely used to assess the densification level of additively manufactured materials. The results for all compositions are reported in Table 11.

*Table 11: result of Archimedes relative density*

| Composition | Sample ID | Porosity Total (%) | Relative Archimedes Density (%) |
|---|---|---|---|
| **316L** | S1 | 0.70 | 99.54 |
| | S2 | 0.46 | 99.62 |
| | S3 | 0.69 | 99.52 |
| | H1 | 0.91 | 99.16 |
| | H2 | 0.91 | 99.36 |
| | H3 | 0.97 | 99.28 |
| **0.1%BN** | S1 | 4.05 | 97.84 |
| | S2 | 4.24 | 97.70 |
| | S3 | 4.87 | 97.25 |
| | H1 | 4.05 | 97.73 |
| | H2 | 3.90 | 97.94 |
| | H3 | 4.14 | 98.04 |
| **0.3%BN** | S1 | 2.91 | 97.73 |
| | S2 | 2.50 | 97.80 |
| | S3 | 2.90 | 97.53 |
| | H1 | 2.75 | 97.66 |
| | H2 | 2.69 | 97.60 |
| | H3 | 2.94 | 97.39 |

All the samples exhibit a relative Archimedes density above 97%, indicating a generally high level of densification. The Archimedes' results highlight a systematic decrease in relative density with BN reinforcement. The 316L reference samples achieved an average density of 99.41 ± 0.18%, confirming near-full densification and excellent process stability. The addition of 0.1% BN reduced the average density to 97.62 ± 0.30%, while 0.3% BN further decreased it slightly to 97.39 ± 0.46%. The higher standard deviation observed in the 0.3% BN group reflects increased variability among specimens, indicating that elevated BN content introduces greater sensitivity to processing conditions. Overall, these results demonstrate that while pure 316L achieves almost full density, BN reinforcement leads to a measurable reduction in densification quality.

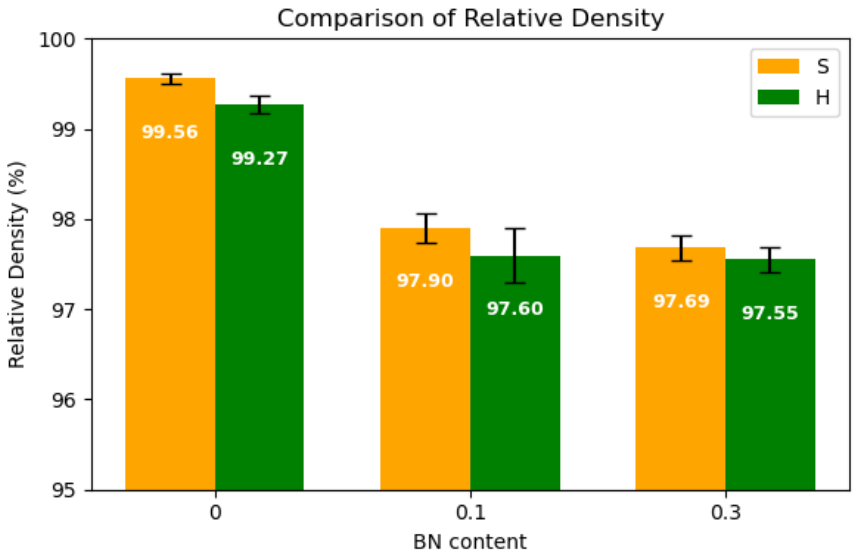


*Figure 43:Effect of reinforcement on relative density of the composite that calculated via Archimedes Density Test*

XCT analysis was performed on the fabricated samples to evaluate their internal structure. In the case of AISI 316L–BN composites, the presence of cracks was confirmed, and their frequency increased with higher BN content. However, these cracks were typically on the microscale and located along grain boundaries. Due to the resolution limitations of the tomography system, such fine cracks could not be clearly detected in the XCT scans. As a result, the analysis primarily reported the porosity distribution of the samples rather than providing a full characterization of the crack network.

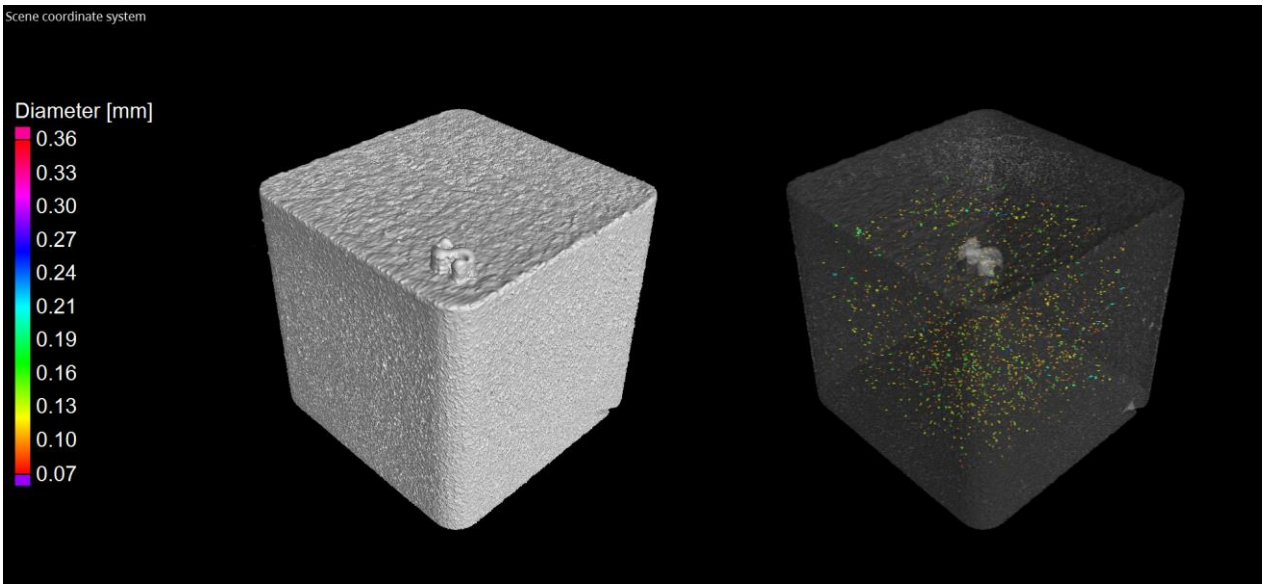

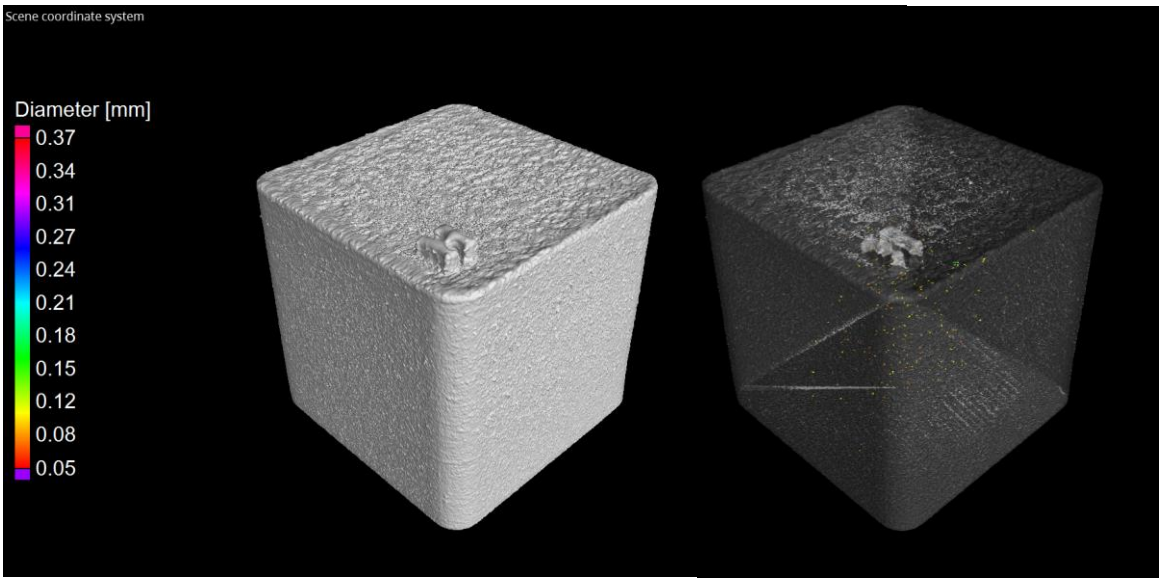


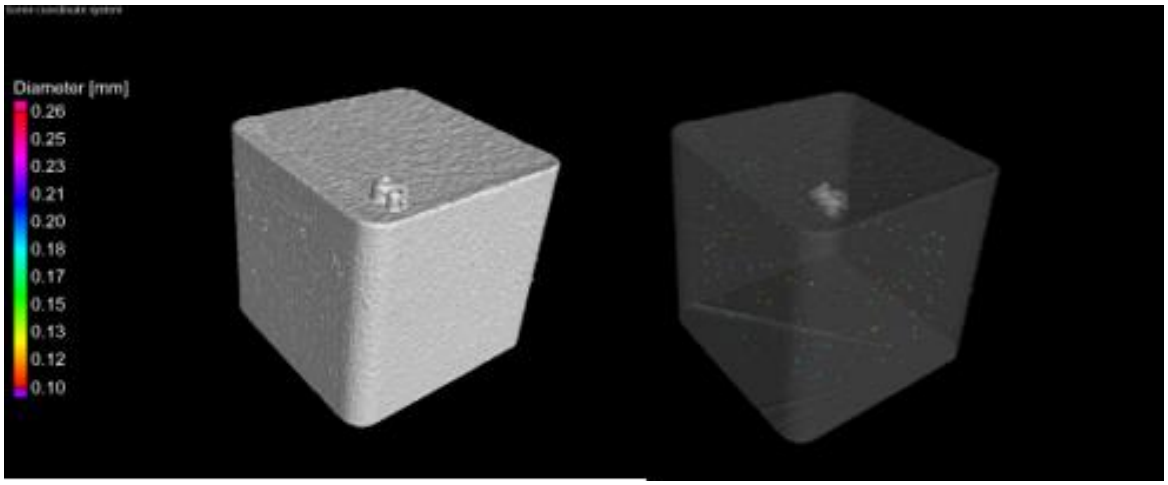


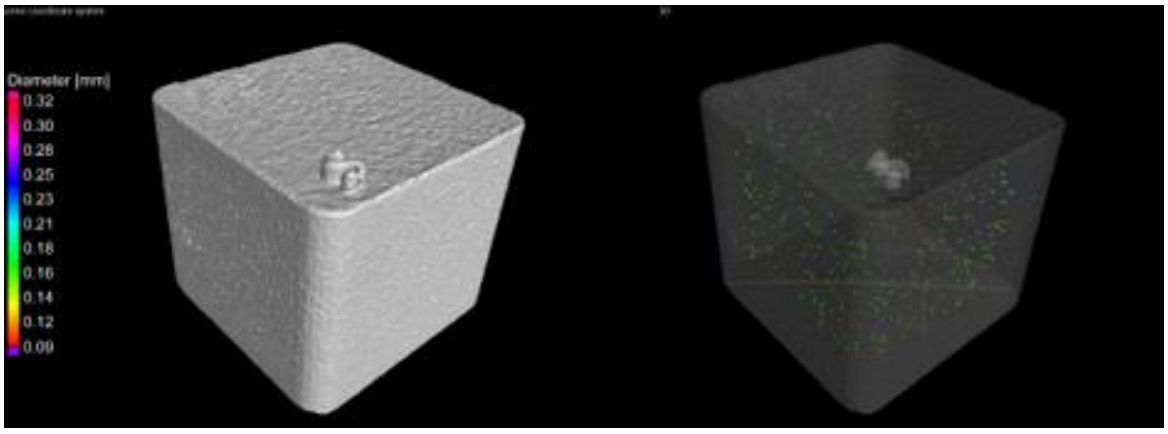


Optical microscopy was used to study the microstructure of the samples and to evaluate their porosity. Images were taken from different regions of each specimen to capture the variation in defect distribution across the surfaces. The porosity density was then estimated using ImageJ software, and the results are presented in the chart. A clear trend was observed: porosity increased with the addition of h-BN. While the base 316L sample showed relatively low porosity, the mixtures with h-BN

exhibited progressively higher values, and in the sample with 3 wt% h-BN, cracks were also detected. This indicates that at higher reinforcement levels, the structural integrity of the material begins to deteriorate.

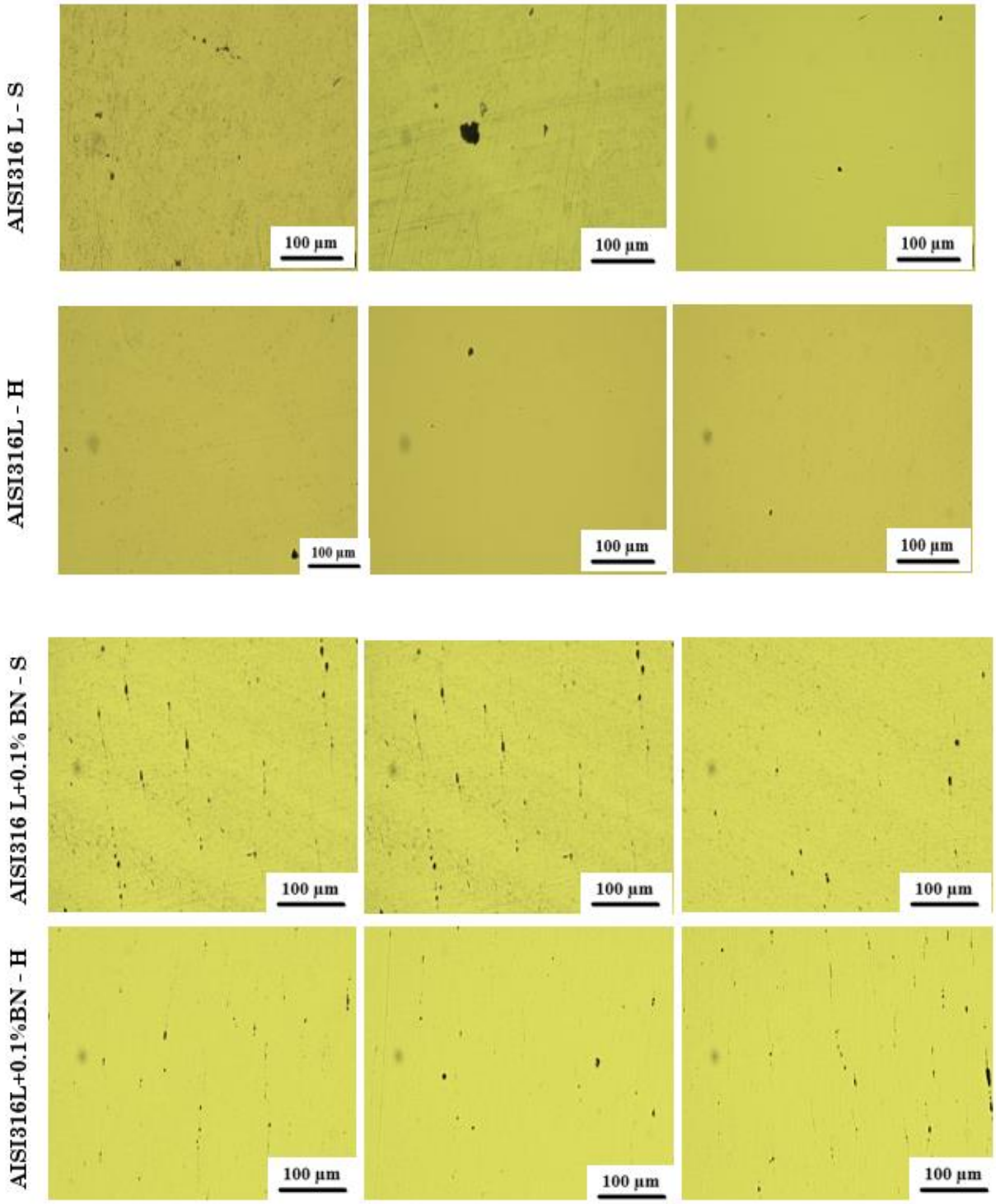

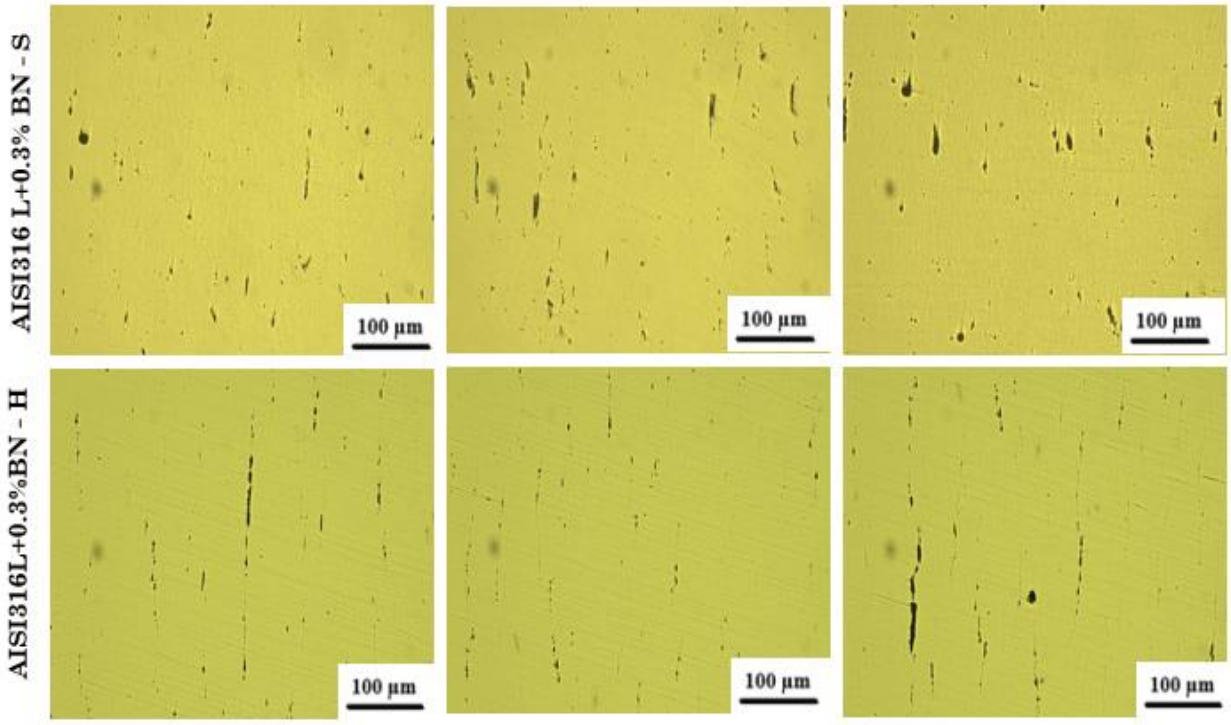


A clear trend was observed: porosity increased with the addition of h-BN. While the base 316L sample showed relatively low porosity, the mixtures with h-BN exhibited progressively higher values, and in the sample with 3 wt% h-BN, cracks were also detected. This indicates that at higher reinforcement levels, the structural integrity of the material begins to deteriorate.

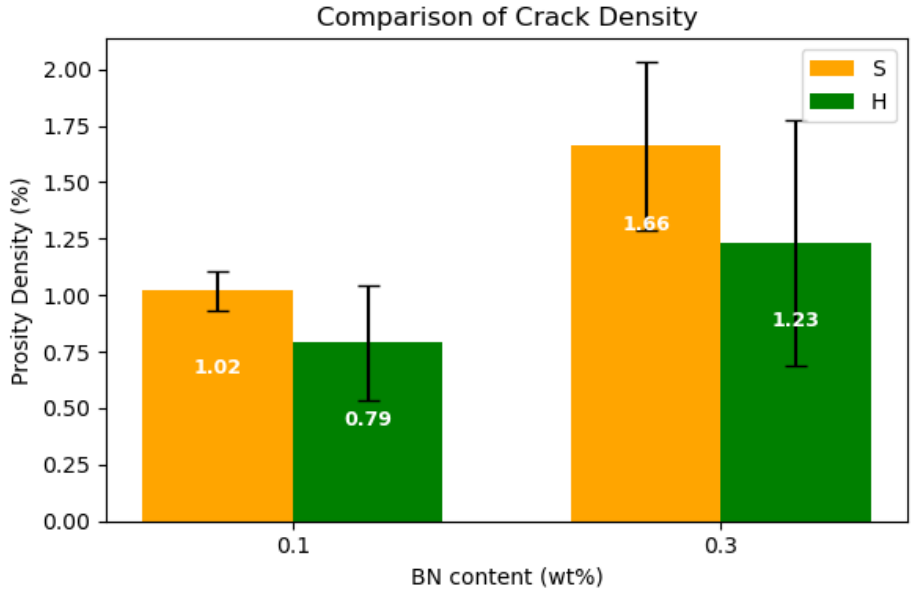

At the same time, it was evident that this method of porosity measurement has limitations. Because defects are not evenly distributed, the results vary depending on which regions are analyzed. This led to relatively large standard deviations in the ImageJ data, highlighting that the method provides only an approximate estimation. Although it captures general trends, it is not highly accurate. For more precise quantification, complementary techniques such as X-ray computed tomography (XCT) would be more reliable, as they provide a complete three-dimensional view of porosity throughout the sample

After etching, the samples were re-examined under an optical microscope, and images were taken from different regions. This allowed a closer observation of the microstructural features and defect distribution. The aim was to report any unusual characteristics or localized irregularities that might not have been visible before etching.

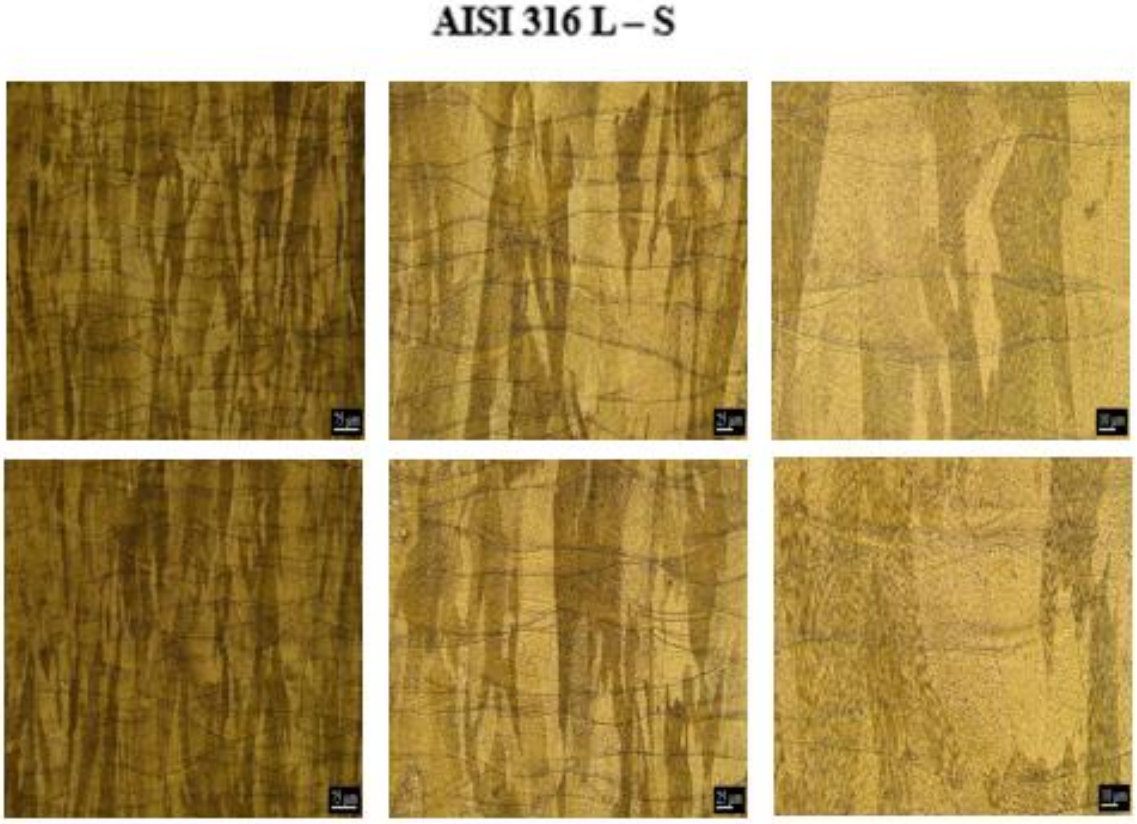


Optical microscopy of the fabricated AISI 316L samples revealed a uniform and defect-free surface, with no evidence of porosity or surface irregularities. This confirms that the selected process

parameters were well-optimized, resulting in a dense structure with good metallurgical bonding between successive layers. The grains observed in the microstructure exhibited a high degree of uniformity, further indicating the stability of the process conditions.

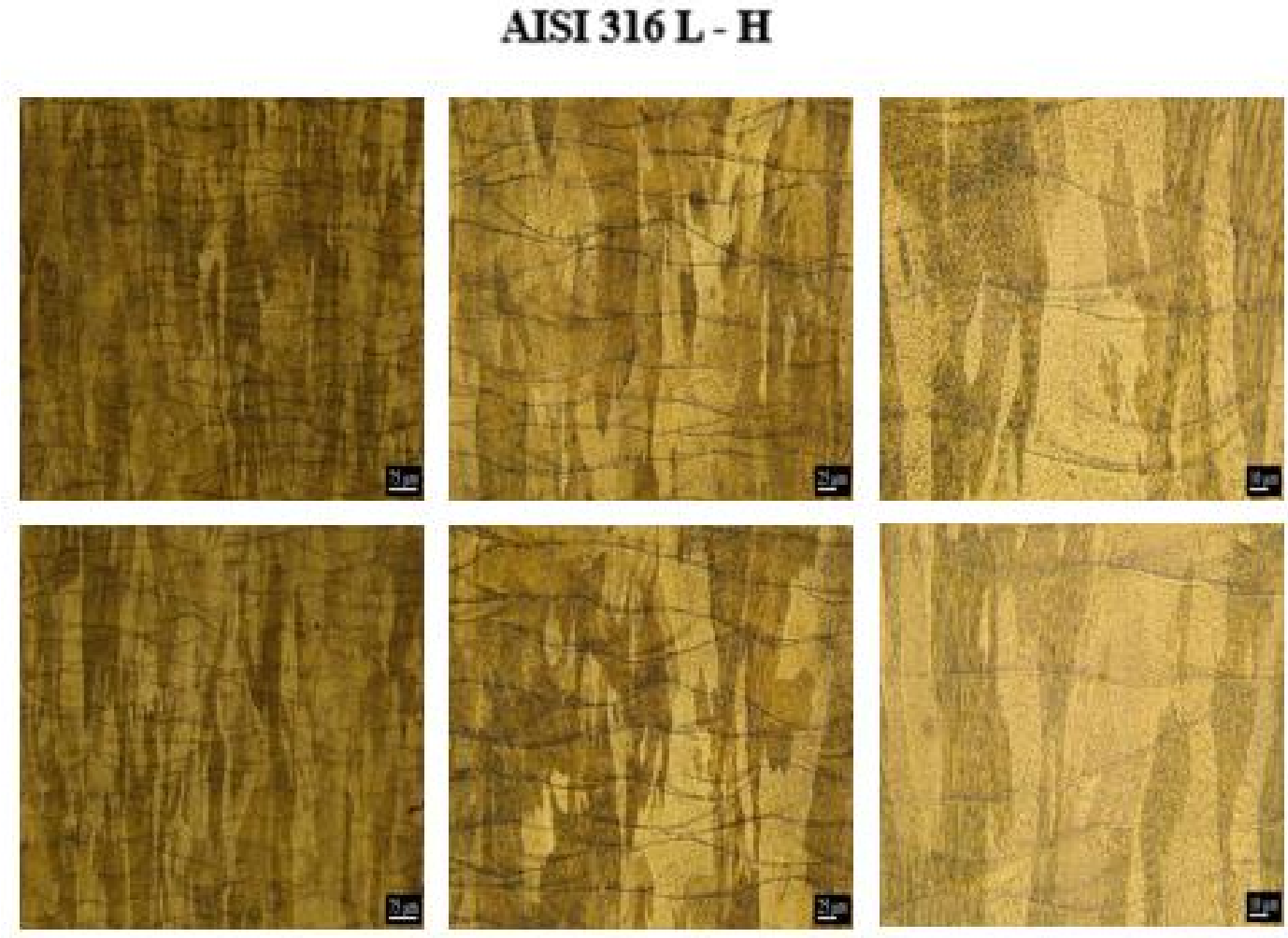


A comparison between samples produced with standard and higher laser energy densities highlights the influence of energy input on grain morphology. At elevated laser energy densities, the melt pool becomes larger and deeper, creating a steeper thermal gradient between the molten zone and the solidified surroundings. In stainless steel 316L, this condition favors directional solidification, where grains preferentially grow along the path of maximum heat flow. Since the strongest gradient is oriented along the build (Z) direction, epitaxial growth from the underlying layers leads to the formation of elongated columnar grains, aligned with the build axis.

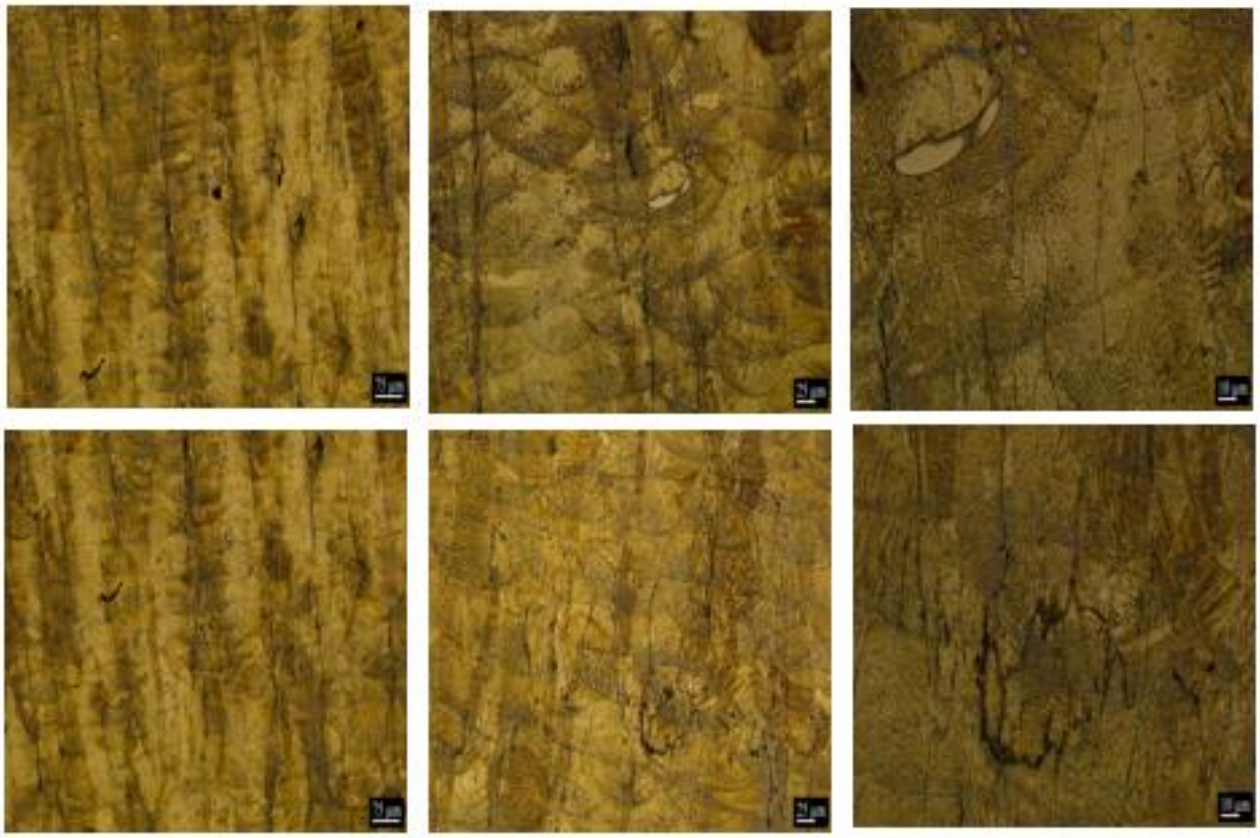


The increase in surface defects after adding 0.1 wt% h-BN is closely related to the nature of this ceramic reinforcement. Because h-BN interacts only weakly with the laser wavelength used in LPBF, it remains unmelted during processing. At the same time, it does not wet stainless steel effectively and has a natural tendency to cluster together. These conditions make it difficult for the particles to be fully incorporated into the melt pool, leading to small lack-of-fusion pores around BN-rich regions and, in some cases, balling or spatter due to disturbed melt flow and locally higher viscosity. In addition, the difference in thermal expansion between h-BN platelets and the steel matrix can create localized stresses during solidification, which may act as initiation points for microcracks along the particle-matrix interface.

**AISI316L + 0.1% BN – H**

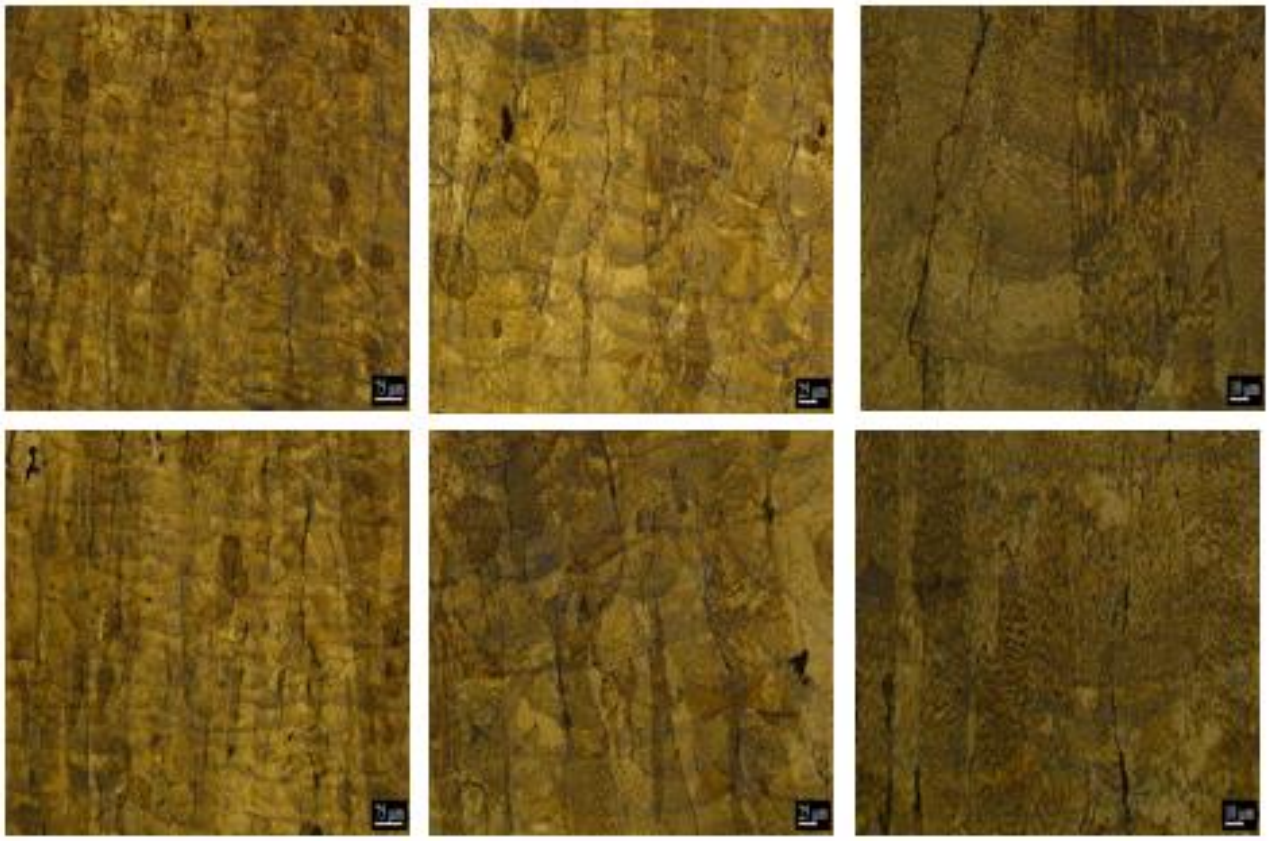

However, when higher laser energy density was applied, the number of visible surface defects decreased slightly compared to the standard energy condition. The deeper and more stable melt pool generated at higher energy improved particle incorporation and interlayer bonding, thereby mitigating, though not eliminating the defect formation associated with BN addition.

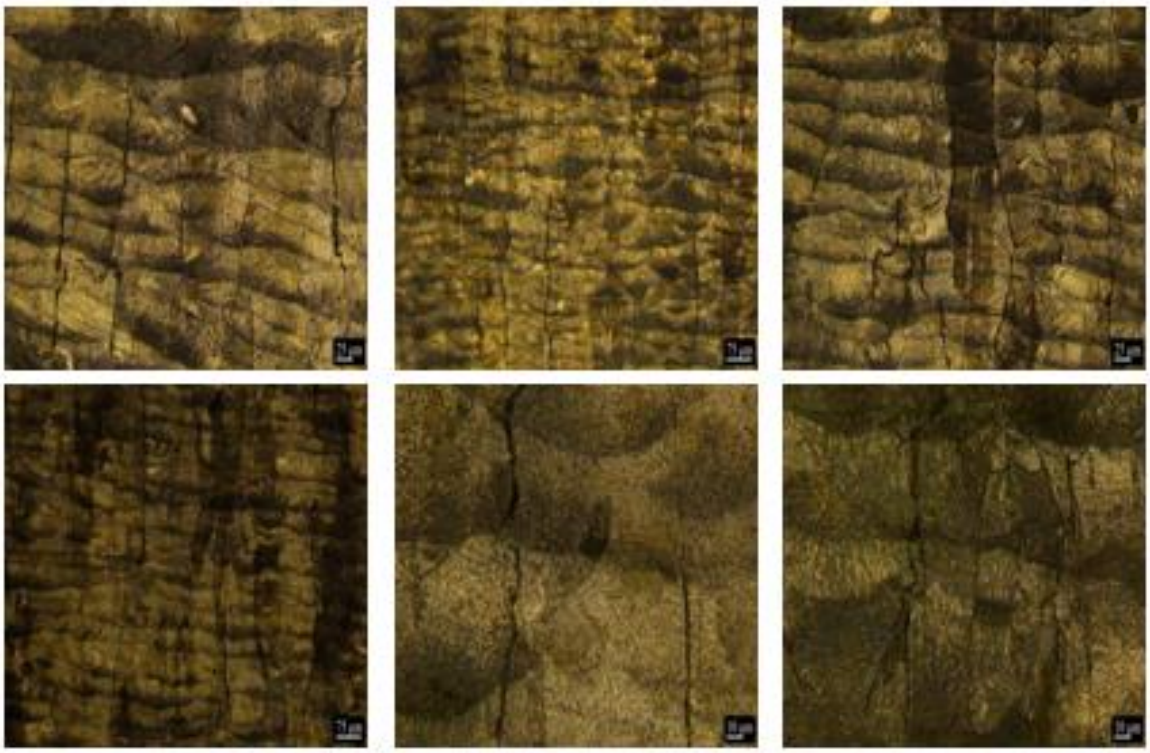


When the h-BN content was further increased to 0.3 wt%, the number of defects in the samples rose even more compared to 0.1 wt%. The higher particle concentration aggravated clustering and incomplete fusion, making it increasingly difficult for the molten steel to fully incorporate the ceramic phase. As a result, both porosity and microstructural irregularities became more pronounced. In addition, the mismatch in thermal expansion between the steel matrix and the h-BN platelets generated greater residual stress during solidification. These stresses, combined with the limited bonding at particle-matrix interfaces, promoted the formation of cracks. Most of these cracks were observed along grain boundaries, which act as natural weak paths in the microstructure and reveal that grain boundaries are especially sensitive to stress concentration under these conditions.

**AISI 316L + 0.3 % BN- H**

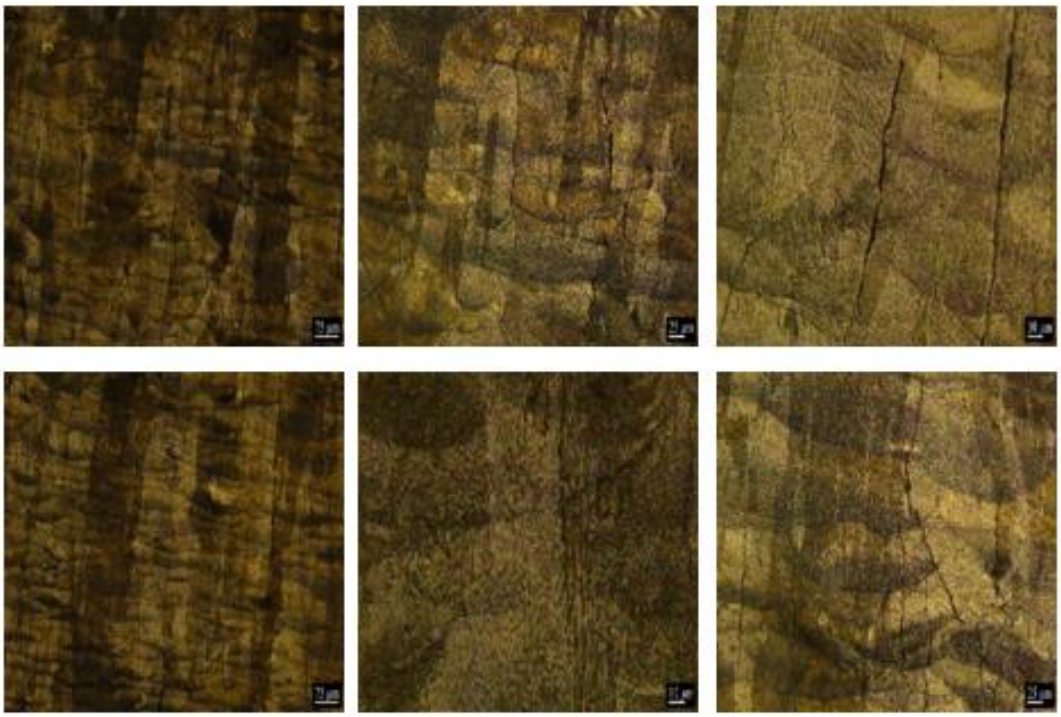

In the table compared the crack density that

In the next step, SEM was used to precisely analyze the type and density of solidification defects. In the 0.1 wt% h-BN sample, the microstructure is relatively homogeneous, with only a few fine pores and isolated cracks observed. In contrast, the 0.3 wt% h-BN sample shows a greater number of solidification-related cracks and voids. Careful observation indicates that most of these cracks are localized along grain boundaries, which represent weak zones formed during rapid cooling in the L-PBF process. The higher reinforcement content appears to intensify these solidification stresses, leading to more pronounced cracking and porosity. These microstructural imperfections can serve as preferential sites for crack initiation under load and are therefore expected to influence the mechanical and wear performance of the material.

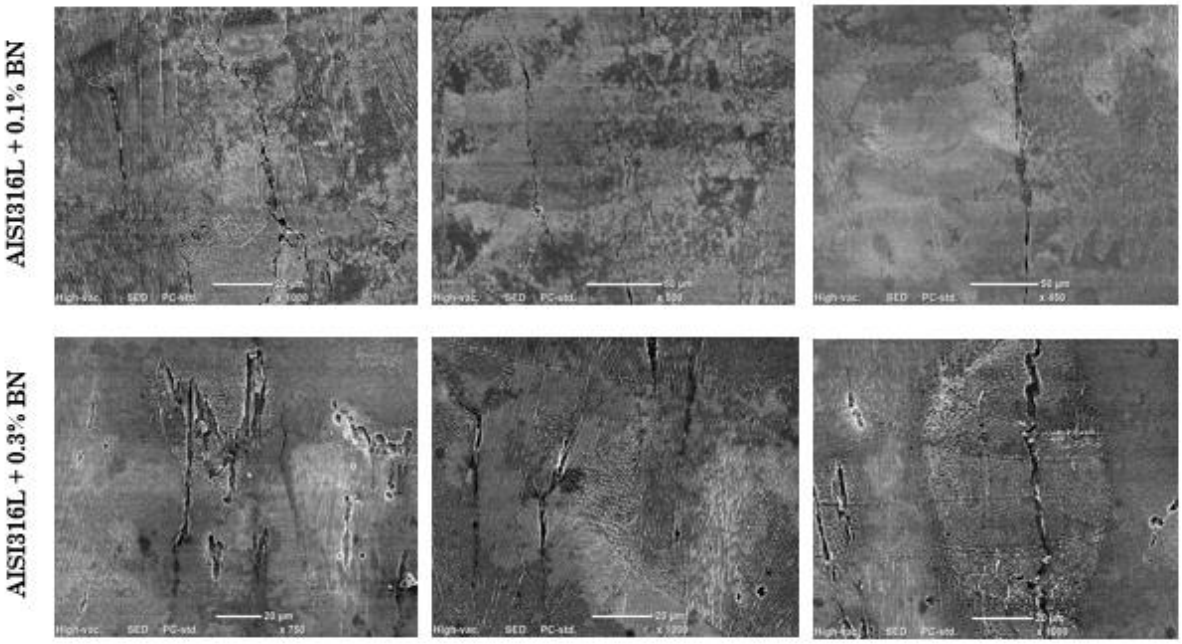


These defects can also be attributed to solidification cracking, which occurs due to the combination of rapid cooling rates and thermal stresses inherent to the L-PBF process. During solidification, shrinkage strains accumulate at the boundaries of growing grains, and when the material is unable to fully accommodate these stresses, cracks form along the grain boundaries. The addition of higher h-BN content further intensifies this effect by disturbing melt pool dynamics and promoting stress concentration, which explains the more pronounced cracking observed in the 0.3 wt% BN sample.

## 4.6. Mechanical Performance Testing

### 4.6.1. Nano Indentation

Nanoindentation testing was performed to evaluate the hardness and elastic modulus of the AISI316L and reinforced samples A Berkovich diamond indenter was applied under controlled loading conditions, and the penetration depth of the tip into the surface was continuously recorded as a function of the applied load. The resulting load–depth curves provide insight into the mechanical response of the material at the micro/nanoscale.

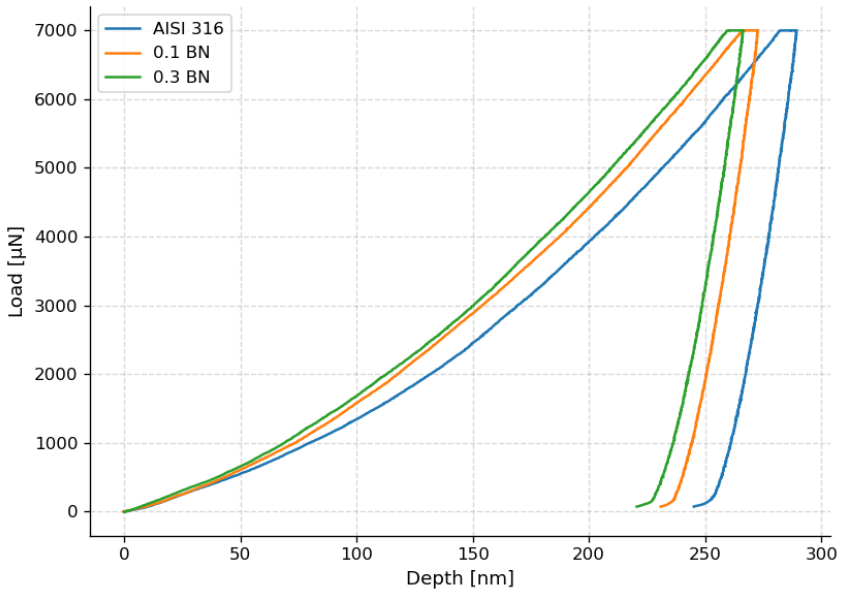


*Figure 44: Load–depth curves from nanoindentation of AISI 316L and h-BN reinforced composites*

The load–depth curves obtained from nanoindentation clearly show the influence of h-BN reinforcement on the mechanical response of the material. The unreinforced 316L sample reached a greater penetration depth (~290 nm) under the same maximum load, indicating lower hardness. In contrast, both the 0.1 wt% and 0.3 wt% h-BN composites exhibited shallower indentation depths (~260–270 nm), confirming their higher resistance to plastic deformation. This behavior demonstrates that the addition of h-BN enhances the hardness and stiffness of the stainless steel matrix, with both reinforced samples showing improved performance compared to the base alloy.

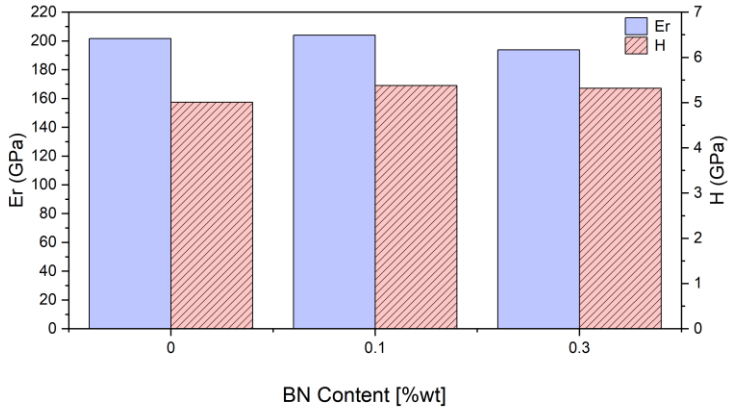

The nanoindentation analysis revealed clear differences in hardness (H) and reduced modulus ($E_r$) with the addition of h-BN. The base 316L exhibited a reduced modulus of about 195 GPa and a hardness of ~5 GPa. With 0.1 wt% h-BN, both values slightly increased, indicating an improvement in stiffness and resistance to plastic deformation. At 0.3 wt% h-BN, the reduced modulus decreased marginally, while hardness remained comparable to the base alloy. This suggests that a small addition of h-BN (0.1 wt%) provides the optimal reinforcing effect, while higher content may introduce defects or microstructural changes that counterbalance the potential gains.

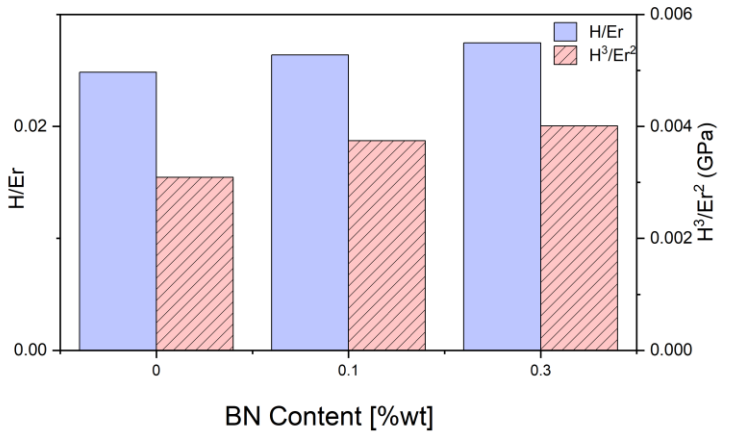


*Figure 45: Wear resistance indicators ($H/E_r$ and $H^3/E_r^2$) of AISI 316L and h-BN reinforced composites from nanoindentation.*

The wear resistance indicators derived from nanoindentation, namely the elastic strain-to-failure ratio ($H/E_r$) and the resistance-to-plastic deformation parameter ($H^3/E_r^2$), further clarify the influence of h-BN. Both parameters increased with the addition of h-BN compared to unreinforced 316L. The 0.1 wt% h-BN composite showed a improvement in both $H/E_r$ and $H^3/E_r^2$, reflecting enhanced elasticity and better resistance to plastic damage. the 0.3 wt% h-BN composite recorded the highest values of both indicators, suggesting superior potential against crack initiation and abrasive wear. These findings are consistent with the observed reduction in friction and weight loss, confirming that h-BN contributes positively to the tribological performance of 316L stainless steel.

### 4.6.2. Wear Test

The wear tests were carried out at room temperature using a zirconia counter-body under a constant applied load of 10 N. The samples were subjected to a total sliding distance of 800 m at a motor speed of 1200 rpm. Three specimens were tested under the same conditions, providing a consistent basis for recording the friction–distance curves and for later calculating the weight loss of each sample.

The friction–distance curves show clear differences between the base 316L and the BN-reinforced powders. The reference 316L sample exhibited the highest average friction coefficient, remaining mostly in the range of 0.76–0.78 throughout the test. With the addition of h-BN, the friction levels decreased. The 0.3 wt% h-BN blend maintained intermediate values (≈0.73–0.75), while the 0.1 wt% h-BN mixture achieved the lowest friction (≈0.70–0.72).

This behavior reflects the solid lubricant effect of h-BN. Lower friction values indicate improved tribological performance, as the BN particles reduce metal-to-metal contact and promote smoother sliding. From these results, it is evident that incorporating h-BN, even at low concentrations, enhances the wear resistance of 316L by lowering the coefficient of friction.

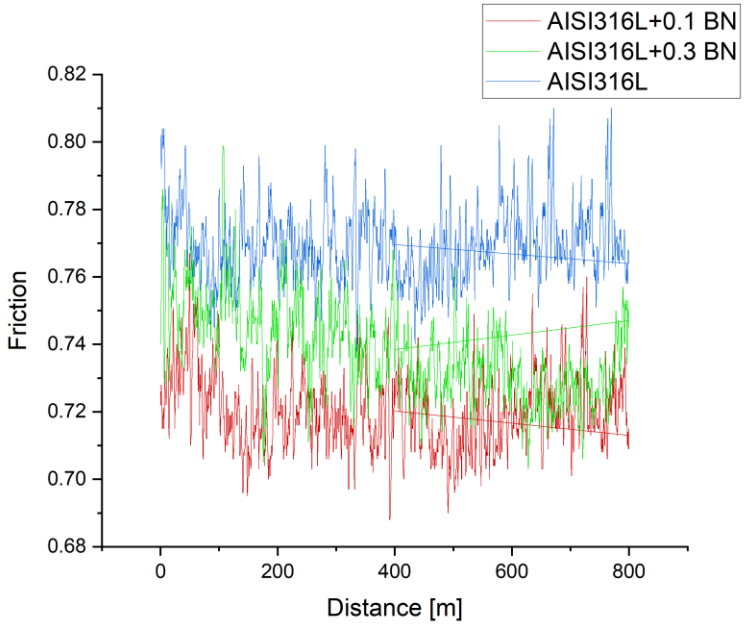


*Figure 46: the friction – distance curve in wear test .*

When the friction coefficient is high, it means there is greater resistance to sliding between the two contact surfaces. This typically causes more surface interaction, leading to higher heat generation, localized stress, and stronger adhesion or plowing effects during sliding. As a result, the material is more prone to surface damage, accelerated material removal, and ultimately higher wear rates.

On the other hand, a lower friction coefficient generally corresponds to smoother sliding, less heat buildup, and reduced abrasive or adhesive interactions. This usually translates into lower wear and longer material life. That is why in tribology, reducing the friction coefficient is often associated with improved wear resistance.

In Table 11. Recorded weight loss of the samples after the wear test, used to evaluate material degradation and wear resistance under applied loading conditions.

*Table 12: Table of weight loose during wear test*

| Sample ID | Initial Weight (g) | Final Weight (g) | Weight Loss (g) |
|---|---|---|---|
| **AISI316L** | 11.1125 | 11.0784 | 0.0341 |
| **AISI316L + 0.1% BN** | 14.4155 | 14.4003 | 0.0152 |
| **AISI316L + 0.3% BN** | 12.7155 | 12.6957 | 0.0198 |

The weight loss measurements after the wear test clearly highlight the beneficial effect of h-BN reinforcement. The unreinforced AISI 316L sample experienced the highest mass loss (0.0341 g), reflecting its lower wear resistance under the applied test conditions. By contrast, the addition of h-BN significantly reduced the material loss: the 0.1 wt% h-BN composite showed the lowest wear with a weight loss of only 0.0152 g, while the 0.3 wt% h-BN composite exhibited a slightly higher but still reduced value of 0.0198 g. These results confirm that h-BN acts as an effective solid lubricant, lowering friction and minimizing material removal during sliding. Interestingly, the 0.1 wt% addition provided the best balance, suggesting that beyond a certain content, the benefits of h-BN may be offset by microstructural changes or higher porosity.

## 5. Conclusion and Future Perspective

In this study, we analyzed the effect of h-BN reinforcement on the AISI 316L matrix, focusing on its influence on microstructure, mechanical properties, and wear behavior. The main findings are summarized in this section.

1. Microstructural analysis confirmed that pure AISI 316L produced under optimized LPBF conditions exhibited a dense and uniform grain structure with almost no visible defects. In contrast, the addition of h-BN progressively increased the occurrence of surface defects and porosity. At 0.1 wt% h-BN, incomplete incorporation of the ceramic phase promoted particle clustering, pores, and localized microcracks, while at 0.3 wt% these imperfections became more pronounced, with cracks predominantly concentrated along grain boundaries due to stress accumulation at particle–matrix interfaces.

2. Mechanical characterization by nanoindentation revealed that the reinforced samples exhibited shallower indentation depths, higher hardness, and improved wear resistance indicators ($H/E_r$ and $H^3/E_r^2$). The 0.3 wt% h-BN addition achieved the highest ratios, indicating greater stiffness and resistance to plastic deformation, whereas the 0.1 wt% addition offered the most balanced overall performance by combining improved mechanical and tribological properties with relatively lower defect density.

3. Wear Testing demonstrated that the addition of h-BN reduced both the coefficient of friction and weight loss compared to unreinforced AISI 316L. The 0.1 wt% reinforcement provided the most favorable balance, while the 0.3 wt% samples still showed improvement but to a slightly lesser degree. These results highlight the effectiveness of h-BN as a solid lubricant in enhancing the wear behavior of LPBF-fabricated 316L.

# 6. References


1. Jamwal A, Agrawal R, Sharma M, Giallanza A. Industry 4.0 technologies for manufacturing sustainability: A systematic review and future research directions. Vol. 11, Applied Sciences (Switzerland). 2021.
2. Gardan J. Additive manufacturing technologies: State of the art and trends. Int J Prod Res. 2016;54(10).
3. Yadroitsev I, Du Plessis A, Yadroitsava I. Basics of laser powder bed fusion. In: Fundamentals of Laser Powder Bed Fusion of Metals. 2021.
4. Ryse R Vande, Edeleva M, Van Stichel O, D'hooge DR, Pille F, Fiorio R, et al. Setting the Optimal Laser Power for Sustainable Powder Bed Fusion Processing of Elastomeric Polyesters: A Combined Experimental and Theoretical Study. Materials. 2022;15(1).
5. Singh R, Gupta A, Tripathi O, Srivastava S, Singh B, Awasthi A, et al. Powder bed fusion process in additive manufacturing: An overview. In: Materials Today: Proceedings. 2019.
6. Carter LN, Martin C, Withers PJ, Attallah MM. The influence of the laser scan strategy on grain structure and cracking behaviour in SLM powder-bed fabricated nickel superalloy. J Alloys Compd. 2014;615.
7. Gillham B, Yankin A, McNamara F, Tomonto C, Taylor D, Lupoi R. Application of the Theory of Critical Distances to predict the effect of induced and process inherent defects for SLM Ti-6Al-4V in high cycle fatigue. CIRP Annals. 2021;70(1).
8. Majeed A, Zhang Y, Lv J, Peng T, Atta Z, Ahmed A. Investigation of T4 and T6 heat treatment influences on relative density and porosity of AlSi10Mg alloy components manufactured by SLM. Comput Ind Eng. 2020;139.
9. Nandhakumar R, Venkatesan K. A process parameters review on selective laser melting-based additive manufacturing of single and multi-material: Microstructure, physical properties, tribological, and surface roughness. Vol. 35, Materials Today Communications. 2023.
10. Gokuldoss PK, Kolla S, Eckert J. Additive manufacturing processes: Selective laser melting, electron beam melting and binder jetting-selection guidelines. Vol. 10, Materials. 2017.
11. Mohan Krishna Sai M, Kumar S, Mandal A, Anand M. Sinterability of SS316, SiC, and TiN multi-material additive manufacturing via selective laser sintering. Opt Laser Technol. 2023;167.
12. Yi Wei a b c GC b, HW c, NT a. High-precision laser powder bed fusion of 316L stainless steel and its SiC reinforcement composite materials. Opt Laser Technol. 2025;

13. Nilsson JO. Can mankind survive without stainless steels? Stainless Steel World. 2014;(December).

14. Aversa A, Saboori A, Marchese G, Iuliano L, Lombardi M, Fino P. Recent Progress in Beam-Based Metal Additive Manufacturing from a Materials Perspective: A Review of Patents. Vol. 30, Journal of Materials Engineering and Performance. 2021.

15. Armstrong M, Mehrabi H, Naveed N. An overview of modern metal additive manufacturing technology. Vol. 84, Journal of Manufacturing Processes. 2022.

16. Yaman U, Butt N, Sacks E, Hoffmann C. Slice coherence in a query-based architecture for 3D heterogeneous printing. CAD Computer Aided Design. 2016;75–76.

17. Moon SK, Tan YE, Hwang J, Yoon YJ. Application of 3D printing technology for designing light-weight unmanned aerial vehicle wing structures. International Journal of Precision Engineering and Manufacturing - Green Technology. 2014;1(3).

18. Pradel P, Zhu Z, Bibb R, Moultrie J. A framework for mapping design for additive manufacturing knowledge for industrial and product design. Journal of Engineering Design. 2018;29(6).

19. Peng X, Kong L, Fuh JYH, Wang H. A review of post-processing technologies in additive manufacturing. Vol. 5, Journal of Manufacturing and Materials Processing. 2021.

20. Armstrong M, Mehrabi H, Naveed N. An overview of modern metal additive manufacturing technology. Vol. 84, Journal of Manufacturing Processes. 2022.

21. Dadkhah M, Tulliani JM, Saboori A, Iuliano L. Additive manufacturing of ceramics: Advances, challenges, and outlook. Vol. 43, Journal of the European Ceramic Society. 2023.

22. Mosallanejad MH, Niroumand B, Aversa A, Saboori A. In-situ alloying in laser-based additive manufacturing processes: A critical review. Vol. 872, Journal of Alloys and Compounds. 2021.

23. Zhai Y, Lados DA, Lagoy JL. Additive Manufacturing: Making imagination the major Limitation. JOM. 2014;66(5).

24. Dilberoglu UM, Gharehpapagh B, Yaman U, Dolen M. The Role of Additive Manufacturing in the Era of Industry 4.0. In: Procedia Manufacturing. 2017.

25. Alghamdi SS, John S, Choudhury NR, Dutta NK. Additive manufacturing of polymer materials: Progress, promise and challenges. Vol. 13, Polymers. 2021.

26. Gardner L. Metal additive manufacturing in structural engineering – review, advances, opportunities and outlook. Vol. 47, Structures. 2023.

27. Li C, Pisignano D, Zhao Y, Xue J. Advances in Medical Applications of Additive Manufacturing. Engineering. 2020;6(11).

28. Prakash KS, Nancharaih T, Rao VVS. Additive Manufacturing Techniques in Manufacturing -An Overview. In: Materials Today: Proceedings. 2018.

29. Collins F. Wohlers Associates. 2014. Wohlers Report 2014 Uncovers Annual Growth of 34.9% for 3D Printing and Additive Manufacturing Industry.

30. Coykendall J, Cotteleer M, Holdowsky J, Mahto M. 3D opportunity in aerospace and defense: Additive manufacturing takes flight. Deloitte University Press. 2014;1.

31. Manish Singla. What are the Advantages and Disadvantages of 3D Printing? Twi-GlobalCom. 2022;

32. ASTM/ISO 52900. Additive manufacturing - General principles - Fundamentals and vocabulary. Vol. 2021, ASTM International. 2021.

33. Mummareddy B, Negro D, Bharambe VT, Oh Y, Burden E, Ahlfors M, et al. Mechanical properties of material jetted zirconia complex geometries with hot isostatic pressing. Advances in Industrial and Manufacturing Engineering. 2021;3.

34. Bidare P, Abdullah R, Jiménez A, Essa K. Powder reusability in Metal Binder Jetting. Proceedings of the Institution of Mechanical Engineers, Part E: Journal of Process Mechanical Engineering. 2024;238(4).

35. Ahn DG. Directed Energy Deposition (DED) Process: State of the Art. Vol. 8, International Journal of Precision Engineering and Manufacturing - Green Technology. 2021.

36. Kok Y, Tan XP, Wang P, Nai MLS, Loh NH, Liu E, et al. Anisotropy and heterogeneity of microstructure and mechanical properties in metal additive manufacturing: A critical review. Mater Des. 2018;139.

37. Tepylo N, Huang X, Patnaik PC. Laser-Based Additive Manufacturing Technologies for Aerospace Applications. Vol. 21, Advanced Engineering Materials. 2019.

38. Zhang LC, Liu Y, Li S, Hao Y. Additive Manufacturing of Titanium Alloys by Electron Beam Melting: A Review. Vol. 20, Advanced Engineering Materials. 2018.

39. Patel R, Desai C, Kushwah S, Mangrola MH. A review article on FDM process parameters in 3D printing for composite materials. Mater Today Proc. 2022;60.

40. Dey A, Eagle INR, Yodo N. A review on filament materials for fused filament fabrication. Vol. 5, Journal of Manufacturing and Materials Processing. 2021.

41. Garcia EA, Ayranci C, Qureshi AJ. Material property-manufacturing process optimization for form 2 VAT-photo polymerization 3D printers. Journal of Manufacturing and Materials Processing. 2020;4(1).

42. Sufiiarov V, Borisov A, Popovich A, Erutin D. Effect of TiC Particle Size on Processing, Microstructure and Mechanical Properties of an Inconel 718/TiC Composite Material Made by Binder Jetting Additive Manufacturing. Metals (Basel). 2023;13(7).

43. Chen Q, Juste E, Lasgorceix M, Petit F, Leriche A. Binder jetting process with ceramic powders: Influence of powder properties and printing parameters. Open Ceramics. 2022;9.

44. Lv X, Ye F, Cheng L, Fan S, Liu Y. Binder jetting of ceramics: Powders, binders, printing parameters, equipment, and post-treatment. Vol. 45, Ceramics International. 2019.

45. Tanabe G, Churei H, Wada T, Takahashi H, Uo M, Ueno T. The influence of temperature on sheet lamination process when fabricating mouthguard on dental thermoforming machine. J Oral Sci. 2020;62(1).

46. Krüger TS, Çabuk O, Maas J. Manufacturing Process for Multilayer Dielectric Elastomer Transducers Based on Sheet-to-Sheet Lamination and Contactless Electrode Application. Actuators. 2023;12(3).

47. Vaughan MW, Elverud M, Ye J, Seede R, Gibbons S, Flater P, et al. Development of a process optimization framework for fabricating fully dense advanced high strength steels using laser directed energy deposition. Addit Manuf. 2023;67.

48. Çallı M, Albak Eİ, Öztürk F. Prediction and Optimization of the Design and Process Parameters of a Hybrid DED Product Using Artificial Intelligence. Applied Sciences (Switzerland). 2022;12(10).

49. Yan Z, Liu W, Tang Z, Liu X, Zhang N, Li M, et al. Review on thermal analysis in laser-based additive manufacturing. Vol. 106, Optics and Laser Technology. 2018.

50. Ribeiro KSB, Mariani FE, Coelho RT. A Study of Different Deposition Strategies in Direct Energy Deposition (DED) Processes. Procedia Manuf. 2020;48.

51. Svetlizky D, Das M, Zheng B, Vyatskikh AL, Bose S, Bandyopadhyay A, et al. Directed energy deposition (DED) additive manufacturing: Physical characteristics, defects, challenges and applications. Vol. 49, Materials Today. 2021.

52. Dass A, Moridi A. State of the art in directed energy deposition: From additive manufacturing to materials design. Vol. 9, Coatings. 2019.

53. Dutta B. Directed Energy Deposition (DED) Technology. In: Encyclopedia of Materials: Metals and Alloys. 2021.

54. Luis Nuñez III CMDIJ van RIC& MRM. Analysis of surface roughness in metal directed energy deposition. The International Journal of Advanced Manufacturing Technology. 2024;

55. Thompson SM, Bian L, Shamsaei N, Yadollahi A. An overview of Direct Laser Deposition for additive manufacturing; Part I: Transport phenomena, modeling and diagnostics. Vol. 8, Additive Manufacturing. 2015.

56. Saboori A, Aversa A, Marchese G, Biamino S, Lombardi M, Fino P. Application of directed energy deposition-based additive manufacturing in repair. Vol. 9, Applied Sciences (Switzerland). 2019.

57. Selcuk C. Laser metal deposition for powder metallurgy parts. Powder Metallurgy. 2011;54(2).

58. Saboori A, Gallo D, Biamino S, Fino P, Lombardi M. An overview of additive manufacturing of titanium components by directed energy deposition: Microstructure and mechanical properties. Vol. 7, Applied Sciences (Switzerland). 2017.

59. Sing SL, Yeong WY. Laser powder bed fusion for metal additive manufacturing: perspectives on recent developments. Vol. 15, Virtual and Physical Prototyping. 2020.

60. Alinejadian N, Kollo L, Odnevall I. Progress in additive manufacturing of MoS2-based structures for energy storage applications – A review. Vol. 139, Materials Science in Semiconductor Processing. 2022.

61. Sefene EM. State-of-the-art of selective laser melting process: A comprehensive review. Vol. 63, Journal of Manufacturing Systems. 2022.

62. Rabin BH, Smolik GR, Korth GE. Characterization of entrapped gases in rapidly solidified powders. Materials Science and Engineering A. 1990;124(1).

63. Reith M, Franke M, Schloffer M, Körner C. Processing 4th generation titanium aluminides via electron beam based additive manufacturing – characterization of microstructure and mechanical properties. Materialia (Oxf). 2020;14.

64. Bhuvanesh Kumar M, Sathiya P. Methods and materials for additive manufacturing: A critical review on advancements and challenges. Vol. 159, Thin-Walled Structures. 2021.

65. Korkmaz ME, Waqar S, Garcia-Collado A, Gupta MK, Krolczyk GM. A technical overview of metallic parts in hybrid additive manufacturing industry. Journal of Materials Research and Technology. 2022;18.

66. Yap CY, Chua CK, Dong ZL, Liu ZH, Zhang DQ, Loh LE, et al. Review of selective laser melting: Materials and applications. Vol. 2, Applied Physics Reviews. 2015.

67. Yap CY, Chua CK, Dong ZL, Liu ZH, Zhang DQ, Loh LE, et al. Review of selective laser melting: Materials and applications APPLIED PHYSICS REVIEWS—FOCUSED REVIEW Review of selective laser melting: Materials and applications. Citation: Appl Phys Rev Appl Phys Rev. 2015;2(101).

68. Sefene EM. State-of-the-art of selective laser melting process: A comprehensive review. Vol. 63, Journal of Manufacturing Systems. Elsevier B.V.; 2022. p. 250–74.

69. Oliveira JP, LaLonde AD, Ma J. Processing parameters in laser powder bed fusion metal additive manufacturing. Mater Des. 2020;193.

70. D'Andrea D. Additive Manufacturing of AISI 316L Stainless Steel: A Review. Vol. 13, Metals. 2023.

71. Gordon J V., Narra SP, Cunningham RW, Liu H, Chen H, Suter RM, et al. Defect structure process maps for laser powder bed fusion additive manufacturing. Addit Manuf. 2020;36.

72. Moussaoui K, Rubio W, Mousseigne M, Sultan T, Rezai F. Effects of Selective Laser Melting additive manufacturing parameters of Inconel 718 on porosity, microstructure and mechanical properties. Materials Science and Engineering: A. 2018;735.

73. Scipioni Bertoli U, Wolfer AJ, Matthews MJ, Delplanque JPR, Schoenung JM. On the limitations of Volumetric Energy Density as a design parameter for Selective Laser Melting. Mater Des. 2017;113.

74. Praneeth J, Venkatesh S, Krishn LS. Process parameters influence on mechanical properties of AlSi10Mg by SLM. Mater Today Proc. 2023;

75. Newell DJ, O'Hara RP, Cobb GR, Palazotto AN, Kirka MM, Burggraf LW, et al. Mitigation of scan strategy effects and material anisotropy through supersolvus annealing in LPBF IN718. Materials Science and Engineering: A. 2019;764.

76. Zou YM, Wu YS, Li KF, Tan CL, Qiu ZG, Zeng DC. Selective laser melting of crack-free Fe-based bulk metallic glass via chessboard scanning strategy. Mater Lett. 2020;272.

77. Jia H, Sun H, Wang H, Wu Y, Wang H. Scanning strategy in selective laser melting (SLM): a review. Vol. 113, International Journal of Advanced Manufacturing Technology. 2021.

78. Liang X, Dong W, Chen Q, To AC. On incorporating scanning strategy effects into the modified inherent strain modeling framework for laser powder bed fusion. Addit Manuf. 2021;37.

79. He Y, Hassanpour A, Bayly AE. Linking particle properties to layer characteristics: Discrete element modelling of cohesive fine powder spreading in additive manufacturing. Addit Manuf. 2020;36.

80. Li Y, Ma C, Qin F, Chen H, Zhao X, Liu R, et al. The microstructure and mechanical properties of 316L austenitic stainless steel prepared by forge and laser melting deposition. Materials Science and Engineering: A. 2023;870.

81. Philip D. Harvey editor, AS for MMPO. Engineering Properties of Steels, . 1982;

82. Metals Handbook, 10th ed., vol. 1, ASM International Handbook Committee., ASM International, Materials Park, OH, . 1990.

83. ASM Metals Handbook. Properties and selection: stainless steels, tool materials and special-purpose metals. in Metals Handbook, Vol 3, 9th edn, ed by D Benjamin, CW Kirkpatrick (ASM International, Metals Park. 1980;

84. AlMangour B, Grzesiak D, Yang JM. In-situ formation of novel TiC-particle-reinforced 316L stainless steel bulk-form composites by selective laser melting. J Alloys Compd. 2017;706.

85. Behjat A, Shamanian M, Iuliano L, Saboori A. Laser powder bed fusion in situ alloying of AISI 316L-2.5%Cu alloy: microstructure and mechanical properties evolution. Progress in Additive Manufacturing. 2024;9(6).

86. Claire Navarre CCMBAMJREL. Tailoring mechanical properties and microstructures in laser powder bed fusion of 316 L stainless steel through aluminium alloying and combined ex-situ and in-situ heat treatments. Addit Manuf. 2025;

87. Kainer KU. Metal Matrix Composites: Custom-made Materials for Automotive and Aerospace Engineering. Metal Matrix Composites: Custom-made Materials for Automotive and Aerospace Engineering. 2006.

88. Moghadam AD, Schultz BF, Ferguson JB, Omrani E, Rohatgi PK, Gupta N. Functional metal matrix composites: Self-lubricating, self-healing, and nanocomposites-an outlook. Vol. 66, JOM. 2014.

89. Ferreira DFS, Miranda G, Oliveira FJ, Oliveira JM. Nano-TiC-reinforced 18Ni300 steel manufactured by Powder Bed Fusion-Laser Beam with improved wear resistance for mould inserts. J Mater Res. 2024;39(1).

90. Haeri S, Benedetti L, Ghita O. Effects of particle elongation on the binary coalescence dynamics of powder grains for Laser Sintering applications. Powder Technol. 2020;363.

91. Vukkum VB, Gupta RK. Review on corrosion performance of laser powder-bed fusion printed 316L stainless steel: Effect of processing parameters, manufacturing defects, post-processing, feedstock, and microstructure. Vol. 221, Materials and Design. 2022.

92. Kamath C, El-Dasher B, Gallegos GF, King WE, Sisto A. Density of additively-manufactured, 316L SS parts using laser powder-bed fusion at powers up to 400 W. International Journal of Advanced Manufacturing Technology. 2014;74(1–4).

93. Holla V, Kopp P, Grünewald J, Wudy K, Kollmannsberger S. Laser beam shape optimization in powder bed fusion of metals. Addit Manuf. 2023;72.

94. Dutt AK, Bansal GK, Tripathy S, Gopala Krishna K, Srivastava VC, Ghosh Chowdhury S. Optimization of Selective Laser Melting (SLM) Additive Manufacturing Process Parameters of 316L Austenitic Stainless Steel. Transactions of the Indian Institute of Metals. 2023;76(2).

95. Salman OO, Funk A, Waske A, Eckert J, Scudino S. Additive Manufacturing of a 316L Steel Matrix Composite Reinforced with CeO2 Particles: Process Optimization by Adjusting the Laser Scanning Speed. Technologies (Basel). 2018;6(1).

96. Yin H, Yang J, Zhang Y, Crilly L, Jackson RL, Lou X. Carbon nanotube (CNT) reinforced 316L stainless steel composites made by laser powder bed fusion: Microstructure and wear response. Wear. 2022;496–497.

97. Li B, Qian B, Xu Y, Liu Z, Zhang J, Xuan F. Additive manufacturing of ultrafine-grained austenitic stainless steel matrix composite via vanadium carbide reinforcement addition and selective laser melting: Formation mechanism and strengthening effect. Materials Science and Engineering: A. 2019;745.

98. Das A, Yadav V, AlMangour B, Prasad HC, Sathish N, Ashiq M, et al. Additive manufacturing of graphene reinforced 316L stainless steel composites with tailored microstructure and mechanical properties. Mater Chem Phys. 2023;303.

99. Li N, Li X, Geng W, Zhao L, Zhu G, Wang R, et al. Template synthesis of boron nitride nanotubes in mesoporous silica SBA-15. Mater Lett. 2005;59(8–9).

100. Izyumskaya N, Demchenko DO, Das S, Özgür Ü, Avrutin V, Morkoç H. Recent Development of Boron Nitride towards Electronic Applications. Vol. 3, Advanced Electronic Materials. 2017.

101. Senyk S, Chodkiewicz A, Gocman K, Szczęśniak B, Kałdoński T. Hexagonal Nano and Micro Boron Nitride: Properties and Lubrication Applications. Materials. 2022;15(3).

102. Kaftanoğlu B, Dökmetaş N. An environmentally friendly method of cutting and forming of materials by boron nitride coated tools. International Journal of Sustainable Manufacturing. 2014;3(2).

103. Sung CM, Tai MF. Mechanism of the solvent-assisted graphite to diamond transition under high pressure: implications for the selection of catalysts. High Temperatures-High Pressures. 1995;27/28(5).

104. Wentorf RH, DeVries RC, Bundy FP. Sintered superhard materials. Science (1979). 1980;208(4446).

105. Zhu PW, Zhao YN, Wang B, He Z, Li DM, Zou GT. Prepared low stress cubic boron nitride film by physical vapor deposition. J Solid State Chem. 2002;167(2).

106. Monteiro SN, Skury ALD, De Azevedo MG, Bobrovnitchii GS. Cubic boron nitride competing with diamond as a superhard engineering material - An overview. Vol. 2, Journal of Materials Research and Technology. 2013.

107. Bao J, Zhu L, Wang H, Han S, Jin Y, Zhao G, et al. Hexagonal Boron Nitride/Blue Phosphorene Heterostructure as a Promising Anode Material for Li/Na-Ion Batteries. Journal of Physical Chemistry C. 2018;122(41).

108. Maity CK, Hatui G, Sahoo S, Saren P, Nayak GC. Boron Nitride based Ternary Nanocomposites with Different Carbonaceous Materials Decorated by Polyaniline for Supercapacitor Application. ChemistrySelect. 2019;4(13).

109. Zhou C, Lai C, Zhang C, Zeng G, Huang D, Cheng M, et al. Semiconductor/boron nitride composites: Synthesis, properties, and photocatalysis applications. Vol. 238, Applied Catalysis B: Environmental. 2018.

110. Zhang K, Feng Y, Wang F, Yang Z, Wang J. Two dimensional hexagonal boron nitride (2D-hBN): Synthesis, properties and applications. Vol. 5, Journal of Materials Chemistry C. 2017.

111. Lu Y, Zhao R, Wang L, E S. Boron nitride nanotubes and nanosheets: Their basic properties, synthesis, and some of applications. Vol. 136, Diamond and Related Materials. 2023.

112. Tay RY, Li H, Wang H, Lin J, Ng ZK, Shivakumar R, et al. Advanced nano boron nitride architectures: Synthesis, properties and emerging applications. Vol. 53, Nano Today. 2023.

113. Gibson I, Rosen DW, Stucker B. Additive manufacturing technologies: Rapid prototyping to direct digital manufacturing. Additive Manufacturing Technologies: Rapid Prototyping to Direct Digital Manufacturing. 2010.

114. Cobbinah PV, Nzeukou RA, Onawale OT, Matizamhuka WR. Laser powder bed fusion of potential superalloys: A review. Vol. 11, Metals. 2021.

115. Slătineanu L, Dodun O, Coteaţă M, Nagîţ G, Băncescu IB, Hriţuc A. Wire electrical discharge machining—a review. Vol. 8, Machines. 2020.

116. Bai S, Perevoshchikova N, Sha Y, Wu X. The effects of selective laser melting process parameters on relative density of the AlSi10Mg parts and suitable procedures of the archimedes method. Applied Sciences (Switzerland). 2019;9(3).

117. Bruce D, Paradise P, Saxena A, Temes S, Clark R, Noe C, et al. A critical assessment of the Archimedes density method for thin-wall specimens in laser powder bed fusion: Measurement capability, process sensitivity and property correlation. J Manuf Process. 2022;79.

118. Obaton AF, Lê M, Prezza V, Marlot D, Delvart P, Huskic A, et al. Investigation of new volumetric non-destructive techniques to characterise additive manufacturing parts. Welding in the World. 2018;62(5).

119. ASTM International. Standard Test Methods for Density of Compacted or Sintered Powder Metallurgy (PM) Products Using Archimedes' Principle. Astm B962-13. 2013;i.

120. Li Y, Linke BS, Voet H, Falk B, Schmitt R, Lam M. Cost, sustainability and surface roughness quality – A comprehensive analysis of products made with personal 3D printers. CIRP J Manuf Sci Technol. 2017;16.

121. Townsend A, Senin N, Blunt L, Leach RK, Taylor JS. Surface texture metrology for metal additive manufacturing: a review. Vol. 46, Precision Engineering. 2016.

122. Withers PJ, Bouman C, Carmignato S, Cnudde V, Grimaldi D, Hagen CK, et al. X-ray computed tomography. Vol. 1, Nature Reviews Methods Primers. 2021.

123. Garcea SC, Wang Y, Withers PJ. X-ray computed tomography of polymer composites. Vol. 156, Composites Science and Technology. 2018.

124. Bunaciu AA, Udriştioiu E gabriela, Aboul-Enein HY. X-Ray Diffraction: Instrumentation and Applications. Vol. 45, Critical Reviews in Analytical Chemistry. 2015.

125. Bär F, Berger L, Jauer L, Kurtuldu G, Schäublin R, Schleifenbaum JH, et al. Laser additive manufacturing of biodegradable magnesium alloy WE43: A detailed microstructure analysis. Acta Biomater. 2019;98.

126. Idris AM, El-Zahhar AA. Indicative properties measurements by SEM, SEM-EDX and XRD for initial homogeneity tests of new certified reference materials. Microchemical Journal. 2019 May 1;146:429–33.

127. Girão AV, Caputo G, Ferro MC. Application of Scanning Electron Microscopy–Energy Dispersive X-Ray Spectroscopy (SEM-EDS). Comprehensive Analytical Chemistry. 2017;75.

128. Nguyen VL, Kim EA, Lee SR, Yun J, Choe J, Yang DY, et al. Evaluation of strain-rate sensitivity of selective laser melted H13 tool steel using nanoindentation tests. Metals (Basel). 2018;8(8).

129. Wang YM, Voisin T, McKeown JT, Ye J, Calta NP, Li Z, et al. Additively manufactured hierarchical stainless steels with high strength and ductility. Nat Mater. 2018;17(1).

130. Uddin MJ, Ramirez-Cedillo E, Mirshams RA, Siller HR. Nanoindentation and electron backscatter diffraction mapping in laser powder bed fusion of stainless steel 316L. Mater Charact. 2021;174.

131. Oyen ML, Cook RF. A practical guide for analysis of nanoindentation data. J Mech Behav Biomed Mater. 2009;2(4).

132. Yang C, Xiong Y, Wang J, Li Y, Jiang W. Mechanical characterization of shale matrix minerals using phase-positioned nanoindentation and nano-dynamic mechanical analysis. Int J Coal Geol. 2020;229.

133. Fischer-Cripps AC. Critical review of analysis and interpretation of nanoindentation test data. Vol. 200, Surface and Coatings Technology. 2006.

134. Leyland A, Matthews A. On the significance of the H/E ratio in wear control: A nanocomposite coating approach to optimised tribological behaviour. Wear. 2000;246(1–2).